Available online at www.sciencedirect.com
ScienceDirect
Journal of Computational Physics 225 (2007) 1100–1124
JOURNAL OF COMPUTATIONAL PHYSICS
www.elsevier.com/locate/jcp

A transient higher order compact scheme for incompressible viscous flows on geometries beyond rectangular

Swapan K. Pandit *, Jiten C. Kalita, D.C. Dalal

Department of Mathematics, Indian Institute of Technology Guwahati, Guwahati 781 039, India

Received 26 November 2005; received in revised form 16 January 2007; accepted 18 January 2007
Available online 30 January 2007

Abstract

In this paper, we propose an implicit high-order compact (HOC) finite-difference scheme for solving the two-dimensional (2D) unsteady Navier–Stokes (N–S) equations on irregular geometries on orthogonal grids. Our scheme is second order accurate in time and fourth order accurate in space. It is used to solve three pertinent fluid flow problems, namely, the flow decayed by viscosity, the lid-driven square cavity and the flow in a constricted channel. It is seen to efficiently capture both transient and steady-state solutions of the N–S equations with Dirichlet as well as Neumann boundary conditions. Apart from including the good features of HOC schemes, our formulation has the added advantage of capturing transient viscous flows involving free and wall bounded shear layers which invariably contain spatial scale variations. Detailed comparison data produced by the scheme for all the three test cases are provided and compared with analytical as well as established numerical results. Excellent comparison is obtained in all the cases.

Keywords: HOC schemes; N–S equations; Constricted channel; Non-uniform grid; Reynolds number; Transient

1. Introduction

The governing equations representing the 2D unsteady incompressible viscous flow of a fluid are the N–S equations which, in non-dimensional primitive variable formulation, can be written as

$$\frac{\partial u}{\partial x}+\frac{\partial v}{\partial y}=0, \tag{1}$$

$$\frac{\partial u}{\partial t}+u\frac{\partial u}{\partial x}+v\frac{\partial u}{\partial y}=-\frac{\partial P}{\partial x}+\frac{1}{Re}\nabla^2 u, \tag{2}$$

$$\frac{\partial v}{\partial t}+u\frac{\partial v}{\partial x}+v\frac{\partial v}{\partial y}=-\frac{\partial P}{\partial y}+\frac{1}{Re}\nabla^2 v, \tag{3}$$

* Corresponding author. Tel.: +91 361 258 2615; fax: +91 361 258 2649.
E-mail addresses: swapan@iitg.ernet.in (S.K. Pandit), jiten@iitg.ernet.in (J.C. Kalita), durga@iitg.ernet.in (D.C. Dalal).

0021-9991/$ - see front matter
doi:10.1016/j.jcp.2007.01.016

where Re is the Reynolds number, P is the pressure and u, v are the velocity components along x- and y-directions respectively. Alternatively the streamfunction $\psi(x,y,t)$ and the vorticity $\zeta(x,y,t)$ can be defined as

$$u = \frac{\partial \psi}{\partial y}, \quad v = -\frac{\partial \psi}{\partial x}, \tag{4}$$

and

$$\zeta = \frac{\partial v}{\partial x} - \frac{\partial u}{\partial y}. \tag{5}$$

With these, the streamfunction–vorticity (ψ–ζ) form of the N–S Eqs. (1)–(3) can be written as

$$-\frac{\partial^2 \psi}{\partial x^2} - \frac{\partial^2 \psi}{\partial y^2} = \zeta, \tag{6}$$

$$Re\frac{\partial \zeta}{\partial t} - \frac{\partial^2 \zeta}{\partial x^2} - \frac{\partial^2 \zeta}{\partial y^2} + uRe\frac{\partial \zeta}{\partial x} + vRe\frac{\partial \zeta}{\partial y} = 0. \tag{7}$$

This ψ–ζ formulation has major advantages over the primitive variable form: firstly, it satisfies the continuity equation automatically and secondly, it decouples the pressure calculation from the velocity calculation. In the process, it also eliminates two computational difficulties, namely, finding (i) the correct boundary condition for pressure, and (ii) an explicit pressure equation satisfying the incompressibility constraint.

The past few decades have seen the development of many numerical schemes [3,4,7,9,12,16,19,20,22–24,26,27,29,32–34,37,40–43] to solve the N–S equations both in the primitive variables (1)–(3) as well as ψ–ζ ((6) and (7)) formulations. Some of these schemes utilize grid points located only directly adjacent to the node about which the differences are taken resulting in a formula involving a 9-point compact stencil for 2D cases. Off late, HOC finite-difference schemes based on 9-point compact stencil [15,16,19–21,29–32,34,40] for the computation of incompressible viscous flows are gaining popularity because of their advantages associated with high-order accuracy coupled with compact difference stencils. However, majority [15,16,20,21,29,31,32,34] of these HOC approaches on 9-point stencil are confined to steady flow calculations mostly on uniform space grids. As such these schemes could not fully exploit the advantages associated with using non-uniform grids, particularly that of mesh grading to resolve smaller scales in the regions of large gradients in the physical domain. Recently, Spotz and Carey [39], Zhang et al. [12], Kalita et al. [20], and Mancera [34] have developed some HOC schemes on non-uniform grids for the 2D convection–diffusion equations. Of these, the application of first two were limited to only linear problems whereas the third one, which used no transformation from the physical to the computational plane could accurately capture steady incompressible viscous flows governed by N–S equations, however, the last one based on Gupta's [15,16] idea is confined to steady flow calculations. Also, whenever there has been attempts to develop HOC scheme for the transient flows, they are confined invariably to uniform space grids [3,13,15,16,19,30]. Although, there exist solutions [2,27,36] of unsteady N–S equations using higher order schemes on non-uniform grids, these schemes could not be termed as compact in true sense; the stencil used in these schemes extends beyond one step length away from the point about which finite differences are taken.

In the present study we propose an HOC scheme based on 9-point compact stencil for the transient, spatially second order quasi-linear partial differential equation without the mixed-derivative term. The scheme which can be applied to both convection–diffusion and reaction–diffusion equations, can also be easily accommodated into solving equations of the N–S type with slight adjustment of the convection coefficients. It may be noted that application of almost all the schemes mentioned above was confined only to rectangular physical domains. The proposed scheme works equally efficiently on problems described on both rectangular as well as other curvilinear coordinate settings. It is implicit, second order accurate in time and fourth order accurate in space. It handles both Dirichlet and Neumann boundary conditions with ease. To validate the scheme, it is first applied to the problem of flow decayed by viscosity having analytical solutions and, then to the classical lid-driven square cavity problem. However, the power of the scheme is better realized when applied to capture the flow in a constricted channel on complex geometrical settings. We compare our numerical results with both analytical and established numerical results, and excellent match is obtained in all the cases.

The paper is organized in the following way: Section 2 describes the mathematical formulation and the numerical method, Section 3 discusses the solution of algebraic systems, Section 4 deals with the numerical experiments and Section 5, the conclusions.

2. Basic formulations and discretization procedure

All Eqs. (2), (3), (6) and (7) can be put under the same umbrella of the two-dimensional time dependent second order equation

$$l\frac{\partial\phi}{\partial t}+\alpha\frac{\partial^2\phi}{\partial x^2}+\beta\frac{\partial^2\phi}{\partial y^2}+\gamma\frac{\partial\phi}{\partial x}+\nu\frac{\partial\phi}{\partial y}+\omega\phi=\theta, \tag{8}$$

where l is constant and θ is the source term.

2.1. Transformation of the governing equations

We now briefly discuss the transformation

$$x=x(\xi,\eta,t),\quad y=y(\xi,\eta,t), \tag{9}$$

from the physical x–y plane to the computational ξ–η plane which is used to convert a complicated grid into a simple, uniform Cartesian grid. Under this transformation, Eq. (8) becomes

$$l\frac{\partial\hat{\phi}}{\partial t}+a\frac{\partial^2\hat{\phi}}{\partial\xi^2}+g\frac{\partial^2\hat{\phi}}{\partial\xi\partial\eta}+b\frac{\partial^2\hat{\phi}}{\partial\eta^2}+c\frac{\partial\hat{\phi}}{\partial\xi}+d\frac{\partial\hat{\phi}}{\partial\eta}+p\hat{\phi}=f, \tag{10}$$

in the computational plane

$$\begin{aligned}
&a(\xi,\eta,t)=\frac{1}{J^2}(\hat{\beta}x_\eta^2+\hat{\alpha}y_\eta^2);\quad b(\xi,\eta,t)=\frac{1}{J^2}(\hat{\beta}x_\xi^2+\hat{\alpha}y_\xi^2);\\
&c(\xi,\eta,t)=\frac{\hat{\gamma}}{J}y_\eta-\frac{\hat{\nu}}{J}x_\eta+R;\quad d(\xi,\eta,t)=-\frac{\hat{\gamma}}{J}y_\xi+\frac{\hat{\nu}}{J}x_\xi+S;\\
&g(\xi,\eta,t)=\frac{-2}{J^2}(\hat{\alpha}y_\eta y_\xi+\hat{\beta}x_\eta x_\xi);\quad p(\xi,\eta,t)=\hat{\omega}(\xi,\eta,t);\\
&f(\xi,\eta,t)=\hat{\theta}(\xi,\eta,t);
\end{aligned} \tag{11}$$

with

$$\begin{aligned}
R=&\frac{1}{J^3}[-y_\eta((\hat{\beta}x_\eta^2+\hat{\alpha}y_\eta^2)x_{\xi\xi}-2(\hat{\alpha}y_\eta y_\xi+\hat{\beta}x_\eta y_\xi)x_{\xi\eta}+(\hat{\beta}x_\xi^2+\hat{\alpha}y_\xi^2)x_{\eta\eta})\\
&+x_\eta((\hat{\beta}x_\eta^2+\hat{\alpha}y_\eta^2)y_{\xi\xi}-2(\hat{\alpha}y_\eta y_\xi+\hat{\beta}x_\eta x_\xi)y_{\xi\eta}+(\hat{\beta}x_\xi^2+\hat{\alpha}y_\xi^2)y_{\eta\eta})],\\
S=&\frac{1}{J^3}[y_\xi((\hat{\beta}x_\eta^2+\hat{\alpha}y_\eta^2)x_{\xi\xi}-2(\hat{\alpha}y_\eta y_\xi+\hat{\beta}x_\eta x_\xi)x_{\xi\eta}+(\hat{\alpha}y_\xi^2+\hat{\beta}x_\xi^2)x_{\eta\eta})\\
&-x_\xi((\hat{\beta}x_\eta^2+\hat{\alpha}y_\eta^2)y_{\xi\xi}-2(\hat{\alpha}y_\eta y_\xi+\hat{\beta}x_\eta x_\xi)y_{\xi\eta}+(\hat{\beta}y_\xi^2+\hat{\alpha}y_\xi^2)y_{\eta\eta})].
\end{aligned}$$

Here, $J=x_\xi y_\eta-y_\xi x_\eta$; $\hat{\alpha},\hat{\beta},\hat{\gamma},\hat{\nu},\hat{\omega},\hat{\theta}$ are the transformed forms of the coefficients $\alpha,\beta,\gamma,\nu,\omega,\theta$ respectively and $\hat{\phi}(\xi,\eta,t)$ is the transformed form of $\phi(x,y,t)$ in (ξ,η) plane.

2.2. Discretization in the transformed plane

Assuming the transformed domain to be rectangular and constructing on it a uniform rectangular mesh of steps h and k in the ξ- and η-directions respectively, the standard central difference approximation to Eq. (10) at the (i,j)th node is given by

$$l\delta_t^+\hat{\phi}|_{i,j}^n+a_{i,j}\delta_\xi^2\hat{\phi}_{i,j}^n+g_{i,j}\delta_\xi\delta_\eta\hat{\phi}_{i,j}^n+b_{i,j}\delta_\eta^2\hat{\phi}_{i,j}^n+c_{i,j}\delta_\xi\hat{\phi}_{i,j}^n+d_{i,j}\delta_\eta\hat{\phi}_{i,j}^n+p_{i,j}\hat{\phi}_{i,j}^n-T_{i,j}^n=f_{i,j}^n, \tag{12}$$

where $\hat{\phi}_{i,j}$ denotes $\hat{\phi}(\xi_i,\eta_j)$; δ_ξ, δ_ξ^2 and $\delta_\eta, \delta_\eta^2$ are the first and second order central difference operators along ξ- and η-directions respectively, and $\delta_\xi\delta_\eta$ is the mixed second order central difference operator. The truncation error $T_{i,j}^n$ is given by

$$T_{i,j}^n = \frac{h^2}{12}\left[a\frac{\partial^4\hat{\phi}}{\partial\xi^4} + 2g\frac{\partial^4\hat{\phi}}{\partial\xi^3\partial\eta} + 2c\frac{\partial^3\hat{\phi}}{\partial\xi^3}\right]_{i,j}^n + \frac{k^2}{12}\left[b\frac{\partial^4\hat{\phi}}{\partial\eta^4} + 2g\frac{\partial^4\hat{\phi}}{\partial\xi\partial\eta^3} + 2d\frac{\partial^3\hat{\phi}}{\partial\eta^3}\right]_{i,j}^n + \mathrm{O}(\Delta t, h^4, k^4). \tag{13}$$

To obtain a fourth order spatial compact formulation for (12), each of the derivatives of the leading terms of (13) are compactly approximated [32] to $\mathrm{O}(h^2,k^2)$. In order to accomplish this, the original PDE of Eq. (10) is treated as an auxiliary relation that can be differentiated to obtain expressions for higher derivatives. For example, successive differentiation of (10) with respect to ξ yields

$$\frac{\partial^3\hat{\phi}}{\partial\xi^3} = \frac{1}{a}\left[\frac{\partial f}{\partial\xi} - \left(\frac{\partial a}{\partial\xi}+c\right)\frac{\partial^2\hat{\phi}}{\partial\xi^2} - \left(\frac{\partial g}{\partial\xi}+d\right)\frac{\partial^2\hat{\phi}}{\partial\xi\partial\eta} - g\frac{\partial^3\hat{\phi}}{\partial\xi^2\partial\eta} - \frac{\partial b}{\partial\xi}\frac{\partial^2\hat{\phi}}{\partial\eta^2}\right.$$
$$\left. -b\frac{\partial^3\hat{\phi}}{\partial\xi\partial\eta^2} - \frac{\partial c}{\partial\xi}\frac{\partial\hat{\phi}}{\partial\xi} - \frac{\partial d}{\partial\xi}\frac{\partial\hat{\phi}}{\partial\eta} - p\frac{\partial\hat{\phi}}{\partial\xi} - \frac{\partial p}{\partial\xi}\hat{\phi} - l\frac{\partial\widehat{\phi_t}}{\partial\xi}\right] \tag{14}$$

and

$$a\frac{\partial^4\hat{\phi}}{\partial\xi^4} = \frac{\partial^2 f}{\partial\xi^2} - \left(\frac{\partial^2 a}{\partial\xi^2}+2\frac{\partial c}{\partial\xi}\right)\frac{\partial^2\hat{\phi}}{\partial\xi^2} - \left(2\frac{\partial a}{\partial\xi}+c\right)\left[\frac{1}{a}\frac{\partial f}{\partial\xi} - \left(\frac{\partial a}{\partial\xi}+c\right)\frac{\partial^2\hat{\phi}}{\partial\xi^2} - \left(\frac{\partial g}{\partial\xi}+d\right)\frac{\partial^2\hat{\phi}}{\partial\xi\partial\eta} - g\frac{\partial^3\hat{\phi}}{\partial\xi^2\partial\eta}\right.$$
$$\left. -\frac{\partial b}{\partial\xi}\frac{\partial^2\hat{\phi}}{\partial\eta^2} - b\frac{\partial^3\hat{\phi}}{\partial\xi\partial\eta^2} - \frac{\partial c}{\partial\xi}\frac{\partial\hat{\phi}}{\partial\xi} - \frac{\partial d}{\partial\xi}\frac{\partial\hat{\phi}}{\partial\eta} - p\frac{\partial\hat{\phi}}{\partial\xi} - \frac{\partial p}{\partial\xi}\hat{\phi} - l\frac{\partial\widehat{\phi_t}}{\partial\xi}\right] - \left(\frac{\partial^2 g}{\partial\xi^2}+2\frac{\partial d}{\partial\xi}\right)\frac{\partial^2\hat{\phi}}{\partial\xi\partial\eta}$$
$$-\left(2\frac{\partial g}{\partial\xi}+d\right)\frac{\partial^3\hat{\phi}}{\partial\xi^2\partial\eta} - g\frac{\partial^4\hat{\phi}}{\partial\xi^3\partial\eta} - \frac{\partial^2 b}{\partial\xi^2}\frac{\partial^2\hat{\phi}}{\partial\eta^2} - 2\frac{\partial b}{\partial\xi}\frac{\partial^3\hat{\phi}}{\partial\xi\partial\eta^2} - b\frac{\partial^4\hat{\phi}}{\partial\xi^2\partial\eta^2} - \frac{\partial^2 c}{\partial\xi^2}\frac{\partial\hat{\phi}}{\partial\xi} - \frac{\partial^2 d}{\partial\xi^2}\frac{\partial\hat{\phi}}{\partial\eta}$$
$$-p\frac{\partial^2\hat{\phi}}{\partial\xi^2} - 2\frac{\partial p}{\partial\xi}\frac{\partial\hat{\phi}}{\partial\xi} - \frac{\partial^2 p}{\partial\xi^2}\hat{\phi} - l\frac{\partial^2\widehat{\phi_t}}{\partial\xi^2}. \tag{15}$$

Expressions for $\frac{\partial^3\hat{\phi}}{\partial\eta^3}$ and $b\frac{\partial^4\hat{\phi}}{\partial\eta^4}$ can be found in a similar way. It is seen that the expressions for the fourth order derivatives (for example, see Eq. (15)) contain mixed-derivative terms like $\frac{\partial^4\hat{\phi}}{\partial\xi^3\partial\eta}, \frac{\partial^4\hat{\phi}}{\partial\xi\partial\eta^3}$ etc. which cannot be

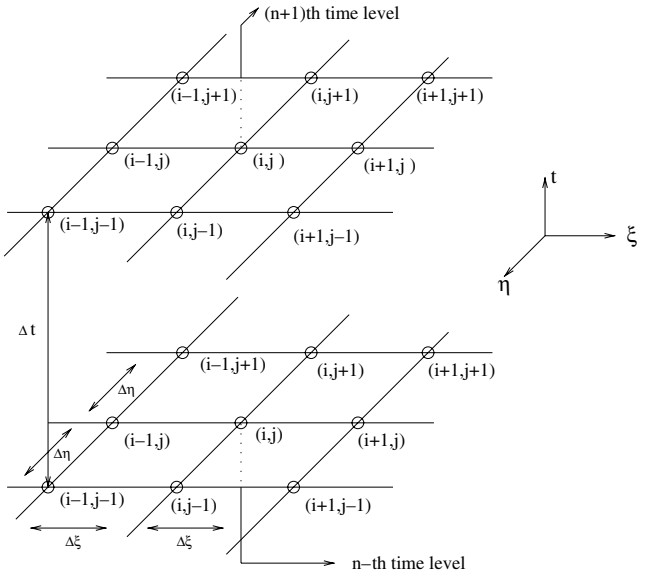

Fig. 1. The unsteady HOC computational (9,9) stencil in $\xi\eta t$-space.

approximated compactly on the stencil shown in Fig. 1. To overcome this difficulty, the transformation can be chosen in such a way that the coefficient g of the mixed-derivative term appearing in Eq. (10) becomes zero. This can be accomplished by choosing an orthogonal grid or conformal mapping [1]. On considering such a grid or transformation, and using central difference for space derivatives and forward temporal difference with uniform step length Δt, Eq. (12) can be written as

$$\begin{aligned} & l\left\{\delta_t^+\hat{\phi}_{i,j}^n + \frac{h^2}{12}(\delta_\xi^2\delta_t^+\hat{\phi}_{i,j}^n + c_{i,j}^*\delta_\xi\delta_t^+\hat{\phi}_{i,j}^n) + \frac{k^2}{12}(\delta_\eta^2\delta_t^+\hat{\phi}_{i,j}^n + d_{i,j}^*\delta_\eta\delta_t^+\hat{\phi}_{i,j}^n)\right\} \\ & \quad + A'_{i,j}\delta_\xi^2\hat{\phi}_{ij}^n + G'_{i,j}\delta_\xi\delta_\eta\hat{\phi}_{i,j}^n + B'_{i,j}\delta_\eta^2\hat{\phi}_{i,j}^n + C'_{i,j}\delta_\xi\hat{\phi}_{i,j}^n + D'_{i,j}\delta_\eta\hat{\phi}_{i,j}^n + H'_{i,j}\hat{\phi}_{i,j}^n \\ & \quad + \frac{1}{12}[(k^2a_{i,j} + h^2b_{i,j})\delta_\xi^2\delta_\eta^2\hat{\phi}_{i,j}^n + \{h^2d_{i,j} + k^2(2\delta_\eta a_{i,j} + d_{i,j}^*a_{i,j})\}\delta_\xi^2\delta_\eta\hat{\phi}_{i,j}^n \\ & \quad + \{k^2c_{i,j} + h^2(2\delta_\xi b_{i,j} + c_{i,j}^*b_{i,j})\}\delta_\xi\delta_\eta^2\hat{\phi}_{i,j}^n] = F''^n_{i,j} + \mathrm{O}(\Delta t, h^4, k^4), \end{aligned} \tag{16}$$

where

$$\begin{aligned} c_{i,j}^* &= \frac{c_{i,j} - 2\delta_\xi a_{i,j}}{a_{i,j}}, \\ d_{i,j}^* &= \frac{d_{i,j} - 2\delta_\eta b_{i,j}}{b_{i,j}}, \\ A'_{i,j} &= a_{i,j} + \frac{h^2}{12}[(\delta_\xi^2 a_{i,j} + 2\delta_\xi c_{i,j} + p_{i,j}) + c_{i,j}^*(\delta_\xi a_{i,j} + c_{i,j})] + \frac{k^2}{12}[d_{i,j}^*\delta_\eta a_{i,j} + \delta_\eta^2 a_{i,j}], \\ B'_{i,j} &= b_{i,j} + \frac{h^2}{12}[c_{i,j}^*\delta_\xi b_{i,j} + \delta_\xi^2 b_{i,j}] + \frac{k^2}{12}[(\delta_\eta^2 b_{i,j} + 2\delta_\eta d_{i,j} + p_{i,j}) + d_{i,j}^*(\delta_\eta b_{i,j} + d_{i,j})], \\ C'_{i,j} &= c_{i,j} + \frac{h^2}{12}[\delta_\xi^2 c_{i,j} + 2\delta_\xi p_{i,j} + c_{i,j}^*(\delta_\xi c_{i,j} + p_{i,j})] + \frac{k^2}{12}[\delta_\eta^2 c_{i,j} + d_{i,j}^*\delta_\eta c_{i,j}], \\ D'_{i,j} &= d_{i,j} + \frac{h^2}{12}[\delta_\xi^2 d_{i,j} + c_{i,j}^*\delta_\xi d_{i,j}] + \frac{k^2}{12}[\delta_\eta^2 d_{i,j} + 2\delta_\eta p_{i,j} + d_{i,j}^*(\delta_\eta d_{i,j} + p_{i,j})], \\ G'_{i,j} &= \frac{h^2}{12}[2\delta_\xi d_{i,j} + c_{i,j}^* d_{i,j}] + \frac{k^2}{12}[2\delta_\eta c_{i,j} + d_{i,j}^* c_{i,j}], \\ H'_{i,j} &= p_{i,j} + \frac{h^2}{12}[\delta_\xi^2 p_{i,j} + c_{i,j}^*\delta_\xi p_{i,j}] + \frac{k^2}{12}[\delta_\eta^2 p_{i,j} + d_{i,j}^*\delta_\eta p_{i,j}], \\ F'_{i,j} &= f_{i,j} + \frac{h^2}{12}[\delta_\xi^2 f_{i,j} + c_{i,j}^*\delta_\xi f_{i,j}] + \frac{k^2}{12}[\delta_\eta^2 f_{i,j} + d_{i,j}^*\delta_\eta f_{i,j}]. \end{aligned}$$

We now introduce a weighted average parameter μ through the approximation of the time derivative $\frac{\partial\hat{\phi}}{\partial t}$ such that $t_\mu = (1-\mu)t^{(n)} + \mu t^{(n+1)}$ where $0 \leqslant \mu \leqslant 1$. Varying μ yields different schemes of different time accuracies. With these, Eq. (16) can be put in the form

$$\sum_{k_1=-1}^{1}\sum_{k_2=-1}^{1} w_{i+k_1,j+k_2}\hat{\phi}_{i+k_1,j+k_2}^{(n+1)} = \sum_{k_1=-1}^{1}\sum_{k_2=-1}^{1} w'_{i+k_1,j+k_2}\hat{\phi}_{i+k_1,j+k_2}^{(n)} + 24\Delta t(\mu F_{i,j}^{(n+1)} + (1-\mu)F_{i,j}^{(n)}), \tag{17}$$

where

$$w_{i+k_1,j+k_2} = \mu\frac{\Delta t}{h^2k^2}r_{i+k_1,j+k_2} + q_{i+k_1,j+k_2}$$

and

$$w'_{i+k_1,j+k_2} = (\mu-1)\frac{\Delta t}{h^2k^2}r_{i+k_1,j+k_2} + q_{i+k_1,j+k_2}$$

with

$$
\begin{aligned}
r_{i-1,j-1} &= (6hkG'_{i,j} + 2X_{i,j} - kY_{i,j} - hZ_{i,j}), \quad q_{i-1,j-1} = 0,\\
r_{i,j-1} &= (24h^2B'_{i,j} - 12h^2kD'_{i,j} - 4X_{i,j} + 2kY_{i,j}), \quad q_{i,j-1} = l(2 - kd^*_{i,j}),\\
r_{i+1,j-1} &= (-6hkG'_{i,j} + 2X_{i,j} - kY_{i,j} + hZ_{i,j}), \quad q_{i+1,j-1} = 0,\\
r_{i-1,j} &= (24k^2A'_{i,j} - 12hk^2C'_{i,j} - 4X_{i,j} + 2hZ_{i,j}), \quad q_{i-1,j} = l(2 - hc^*_{i,j}),\\
r_{i,j} &= (-48k^2A'_{i,j} - 48h^2B'_{i,j} + 24h^2k^2H'_{i,j} + 8X_{i,j}), \quad q_{i,j} = 16l,\\
r_{i+1,j} &= (24k^2A'_{i,j} + 12hk^2C'_{i,j} - 4X_{i,j} - 2hZ_{i,j}), \quad q_{i+1,j} = l(2 + hc^*_{i,j}),\\
r_{i-1,j+1} &= (-6hkG'_{i,j} + 2X_{i,j} + kY_{i,j} - hZ_{i,j}), \quad q_{i-1,j+1} = 0,\\
r_{i,j+1} &= (24h^2B'_{i,j} + 12h^2kD'_{i,j} - 4X_{i,j} - 2kY_{i,j}), \quad q_{i,j+1} = l(2 + kd^*_{ij}),\\
r_{i+1,j+1} &= (6hkG'_{i,j} + 2X_{i,j} + kY_{i,j} + hZ_{i,j}), \quad q_{i+1,j+1} = 0,
\end{aligned}
$$

in which

$$
\begin{aligned}
X_{i,j} &= h^2b_{i,j} + k^2a_{i,j},\\
Y_{i,j} &= h^2d_{i,j} + k^2(2\delta_\eta a_{i,j} + d^*_{i,j}a_{i,j}),\\
Z_{i,j} &= h^2(2\delta_\xi b_{i,j} + c^*_{i,j}b_{i,j}) + k^2c_{i,j}.
\end{aligned}
$$

Thus Eq. (17) becomes the $O((\Delta t)^s, h^4, k^4)$ HOC finite-difference approximation for (10) on the transformed plane. The order of accuracy is preserved in the physical plane if the transformation function is smooth enough [8,18]. Accordingly, we have chosen our transformation function in such a way that the order of accuracy is preserved as can be seen from Tables 2 and 8.

It should be noted that for $\mu = 0$, the computational stencil requires nine points at the nth and five points at $(n+1)$th time level resulting in what may be termed as a $(9,5)$ scheme. Similarly $\mu = 0.5$ and $\mu = 1$ yield a $(9,9)$ and a $(5,9)$ scheme respectively. The temporal order of accuracy s is two for the $(9,9)$ scheme and one for the other two. Throughout our computations, we have used the $(9,9)$ scheme (see the corresponding stencil in Fig. 1).

3. Solution of algebraic systems

We now discuss the solution of algebraic systems associated with the newly proposed finite-difference approximations. The system of Eq. (17) can be written in matrix form as

$$A\mathbf{\Phi}^{n+1} = \mathbf{f}(\mathbf{\Phi}^n), \tag{18}$$

where the coefficient matrix A is an asymmetric sparse matrix. For a grid of size $m \times n$, A has dimension mn, and $\mathbf{\Phi}^{n+1}$ and $\mathbf{f}(\mathbf{\Phi}^n)$ are mn-component vectors.

The next step now is to solve Eq. (17) with iterative methods. As the coefficient matrix A is not generally diagonally dominant, conventional iterative methods such as Gauss–Seidel cannot be used. On uniform grids, some of the associated matrices are symmetric and positive definite, which allows algorithms like conjugate-gradient (CG) [42] to be used. As non-uniform grid invariably leads to non-symmetric matrices, in order to solve these systems the biconjugate-gradient stabilized method (BiCGStab) [42] is used here without preconditioning.

To solve the N–S equations using the proposed scheme, we have used the ψ–ζ formulations and employed an outer-inner iteration procedure. In a typical outer temporal cycle, we solve the transformation of (7) using (17) with $l = Re$, $\alpha = -1$, $\beta = -1$, $\gamma = uRe$, $\nu = vRe$, $\omega = 0$, $\theta = 0$ in (10). Then we solve the transformation of (6) using the steady-state form of (17) with $l = 0$, $\alpha = -1$, $\beta = -1$, $\gamma = 0$, $\nu = 0$, $\omega = 0$, $\theta = \zeta$ in (10). For both the vorticity and streamfunction equation, BiCGStab is used, which constitutes the inner iterations. Once (6) is solved, u and v in (4) can be approximated compactly up to fourth order accuracy using the following HOC form

$$
\begin{aligned}
u_{i,j} = \Bigg[& -\frac{x_\eta}{J}\left\{\delta_\xi\psi - \frac{h^2}{6}\left(\frac{1}{a}[\delta_\xi f - (\delta_\xi a + c)(\delta_\xi^2\psi) - (\delta_\xi g + d)(\delta_\xi\delta_\eta\psi) - g(\delta_\xi^2\delta_\eta\psi) - (\delta_\xi b)(\delta_\eta^2\psi)\right.\right. \\
& \left.\left. -b(\delta_\xi\delta_\eta^2\psi) - (\delta_\xi c)(\delta_\xi\psi) - (\delta_\xi d)(\delta_\eta\psi) - p(\delta_\xi\psi) - \psi(\delta_\xi p)]\right)\right\} \\
& + \frac{x_\xi}{J}\left\{\delta_\eta\psi - \frac{k^2}{6}\left(\frac{1}{b}[\delta_\eta f - (\delta_\eta b + d)(\delta_\eta^2\psi) - (\delta_\eta g + c)(\delta_\xi\delta_\eta\psi) - g(\delta_\xi\delta_\eta^2\psi)\right.\right. \\
& \left.\left. -(\delta_\eta a)(\delta_\xi^2\psi) - a(\delta_\xi^2\delta_\eta\psi) - (\delta_\eta c)(\delta_\xi\psi) - (\delta_\eta d)(\delta_\eta\psi) - p(\delta_\eta\psi) - \psi(\delta_\eta p)]\right)\right\}\Bigg]_{i,j} + \mathrm{O}(h^4, k^4), \\
v_{i,j} = \Bigg[& -\frac{y_\eta}{J}\left\{\delta_\xi\psi - \frac{h^2}{6}\left(\frac{1}{a}\left[\delta_\xi f - (\delta_\xi a + c)(\delta_\xi^2\psi) - (\delta_\xi g + d)(\delta_\xi\delta_\eta\psi) - g(\delta_\xi^2\delta_\eta\psi) - (\delta_\xi b)(\delta_\eta^2\psi)\right.\right.\right. \\
& \left.\left.\left. -b(\delta_\xi\delta_\eta^2\psi) - (\delta_\xi c)(\delta_\xi\psi) - (\delta_\xi d)(\delta_\eta\psi) - p(\delta_\xi\psi) - \psi(\delta_\xi p)\right]\right)\right\} \\
& + \frac{y_\xi}{J}\left\{\delta_\eta\psi - \frac{k^2}{6}\left(\frac{1}{b}\left[\delta_\eta f - (\delta_\eta b + d)(\delta_\eta^2\psi) - (\delta_\eta g + c)(\delta_\xi\delta_\eta\psi) - g(\delta_\xi\delta_\eta^2\psi) - (\delta_\eta a)(\delta_\xi^2\psi)\right.\right.\right. \\
& \left.\left.\left. -a(\delta_\xi^2\delta_\eta\psi) - (\delta_\eta c)(\delta_\xi\psi) - (\delta_\eta d)(\delta_\eta\psi) - p(\delta_\eta\psi) - \psi(\delta_\eta p)\right]\right)\right\}\Bigg]_{i,j} + \mathrm{O}(h^4, k^4),
\end{aligned}
\tag{19}
$$

where the expressions for a, b, c, d, g can be calculated from (11), and p and f are the transformed coefficients of ω and θ respectively in ξ–η plane when the transformed equation of (6) acts as Eq. (10). This completes one outer iteration cycle. We utilize a relaxation parameter ϵ for the inner iteration cycles for both ζ and ψ. For larger values of Reynolds number, we need smaller values of ϵ. All of our computations were carried out on a Pentium 4 based PC with 512 MB RAM.

4. Numerical test cases

In order to study the validity and effectiveness of the proposed scheme, it is applied to three unsteady 2D problems. These are (i) the flow decayed by viscosity, (ii) the lid-driven cavity flow and (iii) the flow in a constricted channel. Problem (i) has analytical solutions, so Dirichlet boundary conditions are used for it while for the remaining two, we use both Dirichlet and Neumann boundary conditions. For the first problem, we use exact initial data; for the other two, steady-state solution is computed in a time-marching fashion, and zero initial data was used in all the computations.

4.1. Test case 1

Firstly we consider the problem of flow decayed by viscosity [10,21,41,44] governed by Eqs. (1)–(3) in the square $0 \leqslant x,\ y \leqslant \pi$ with the following initial conditions

$$u(x, y, 0) = -\cos(x)\sin(y) \quad \text{and} \quad v(x, y, 0) = \sin(x)\cos(y). \tag{20}$$

The exact solution of this problem is given by

$$u(x, y, t) = -\cos(x)\sin(y)\mathrm{e}^{-\frac{2t}{Re}} \quad \text{and} \quad v(x, y, t) = \sin(x)\cos(y)\mathrm{e}^{-\frac{2t}{Re}}. \tag{21}$$

The initial and boundary conditions for the ψ–ζ formulations of these equations can be easily derived from the exact solution.

As the flow is characterized by a number of free shear layers, in order to resolve the flow accurately, we have generated the grid in such a way (see Fig. 2) that maximum number of points gets allocated to those regions. To generate the grid we have used the following stretching functions:

$$x = \xi - \frac{\lambda}{4}\sin(4\xi), \quad y = \eta - \frac{\lambda}{4}\sin(4\eta).$$

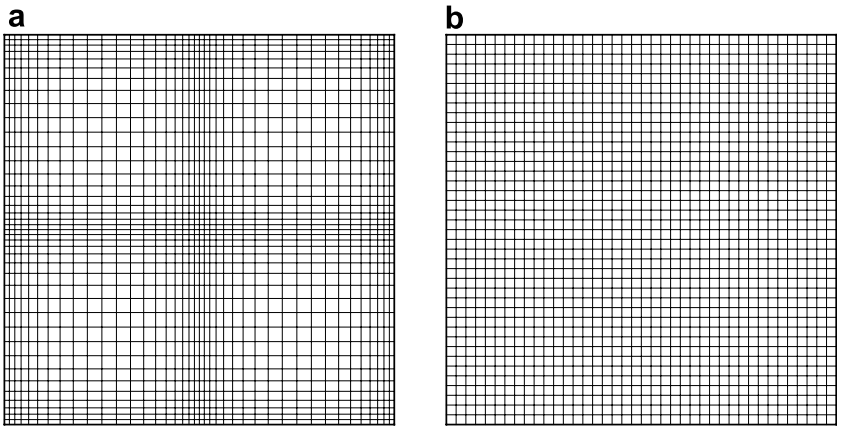

Fig. 2. For problem 1: 41×41 grids: (a) physical plane ($\lambda = 0.5$) and (b) computational plane.

Here, the parameter $\lambda \in [0,1)$ determines the degree of clustering; note that a larger value of λ indicates more grid points at specified locations. The stretching functions generate a centro-symmetric distribution of points with clustering in the vicinity of the horizontal and vertical centerlines.

We present our results computed on different grid sizes for different Reynolds number in Tables 1, 2 and Fig. 3. In Table 1(a), we show the values of ψ, ζ for time $t = 1.0$ and 10.0 at the point $\left(\frac{\pi}{4}, \frac{\pi}{10}\right)$, whereas Table 1(b) shows variation in u and v with respect to time (t). It is obvious from the table that our numerical results are grid independent and they are in excellent agreement with the analytical ones. In Fig. 3(a) and (b), we show the numerical and analytical streamlines for $Re = 1000$ on a 81×81 grid and Fig. 3(c) and (d) show the corresponding vorticity contours at time $t = 10.0$ for the same Reynolds number. All these figures indicate a very close match of the numerical solutions with the exact ones including excellent resolution of the shear layers. In Table 2, we present the maximum absolute errors of ψ, ζ, u and v for $Re = 100$ on three different grid sizes 21×21, 41×41 and 81×81 at $t = 10.0$. This table clearly demonstrates that with grid refinement, the error decays with $O(h^4)$ as expected.

Table 1
Grid independence study for problem 1: numerical and exact values of ψ, ζ, u and v at the point $(\frac{\pi}{4}, \frac{\pi}{10})$ for different Res at different time stations $t = 1$, 10 and grid sizes with $\Delta t = 0.01$ and $\lambda = 0.5$

t	Re	Stream-function (ψ)			Exact	Vorticity (ζ)			Exact
		21×21	41×41	81×81		21×21	41×41	81×81	
(a)									
1.0	100	0.680621	0.679970	0.679934	0.679932	1.361058	1.359910	1.359866	1.359864
	400	0.691508	0.690313	0.690214	0.690208	1.385520	1.380628	1.380417	1.380416
	1000	0.693919	0.692480	0.692296	0.692282	1.394472	1.385375	1.384579	1.384563
10.0	100	0.568445	0.567849	0.567815	0.567813	1.136711	1.135682	1.135630	1.135627
	400	0.660942	0.659928	0.659811	0.659804	1.323536	1.319808	1.319613	1.319608
	1000	0.681361	0.680119	0.679937	0.679918	1.368113	1.360586	1.359864	1.359837
		Velocity (u)				Velocity (v)			
(b)									
1.0	100	−0.129682	−0.134237	−0.134474	−0.134489	0.682061	0.680064	0.679940	0.679932
	400	−0.128669	−0.135917	−0.136486	−0.136522	0.692395	0.690369	0.690219	0.690208
	1000	−0.127638	−0.135865	−0.136851	−0.136932	0.694413	0.692454	0.692296	0.692282
10.0	100	−0.108007	−0.112084	−0.112299	−0.112312	0.569634	0.567926	0.567820	0.567813
	400	−0.123506	−0.129804	−0.130466	−0.130508	0.661914	0.659969	0.659815	0.659804
	1000	−0.126156	−0.133403	−0.134383	−0.134486	0.682178	0.680092	0.679935	0.679918

Table 2
Problem 1: maximum absolute errors and convergence rates of ψ, ζ, u and v for $Re = 100$ at two time stations $t = 1$ and $t = 10$ ($\Delta t = 0.01$ and $\lambda = 0.5$)

t	Grid	ψ Max (ψ)	Rate (ψ)
(a)			
1.0	21×21	1.367266(−3)	
			3.99
	41×41	8.604717(−5)	
			4.04
	81×81	5.222722(−6)	
10.0	21×21	1.480007(−3)	
			3.99
	41×41	9.345349(−5)	
			4.05
	81×81	5.646347(−6)	
		ζ	Rate (ζ)
(b)		Max (ζ)	
1.0	21×21	9.765736(−3)	
			3.89
	41×41	6.572612(−4)	
			4.01
	81×81	4.070853(−5)	
10.0	21×21	1.150130(−2)	
			3.83
	41×41	8.085744(−4)	
			4.02
	81×81	4.990446(−5)	
		u	Rate (u)
(c)		Max (u)	
1.0	21×21	2.185866(−2)	
			3.53
	41×41	1.890278(−3)	
			3.83
	81×81	1.328059(−4)	
10.0	21×21	1.871943(−2)	
			3.55
	41×41	1.596069(−3)	
			3.84
	81×81	1.114534(−4)	
		v	Rate (v)
(d)		Max (v)	
1.0	21×21	2.166603(−2)	
			3.53
	41×41	1.877177(−3)	
			3.83
	81×81	1.323446(−4)	
10.0	21×21	1.812902(−2)	
			3.53
	41×41	1.569013(−3)	
			3.83
	81×81	1.105766(−4)	

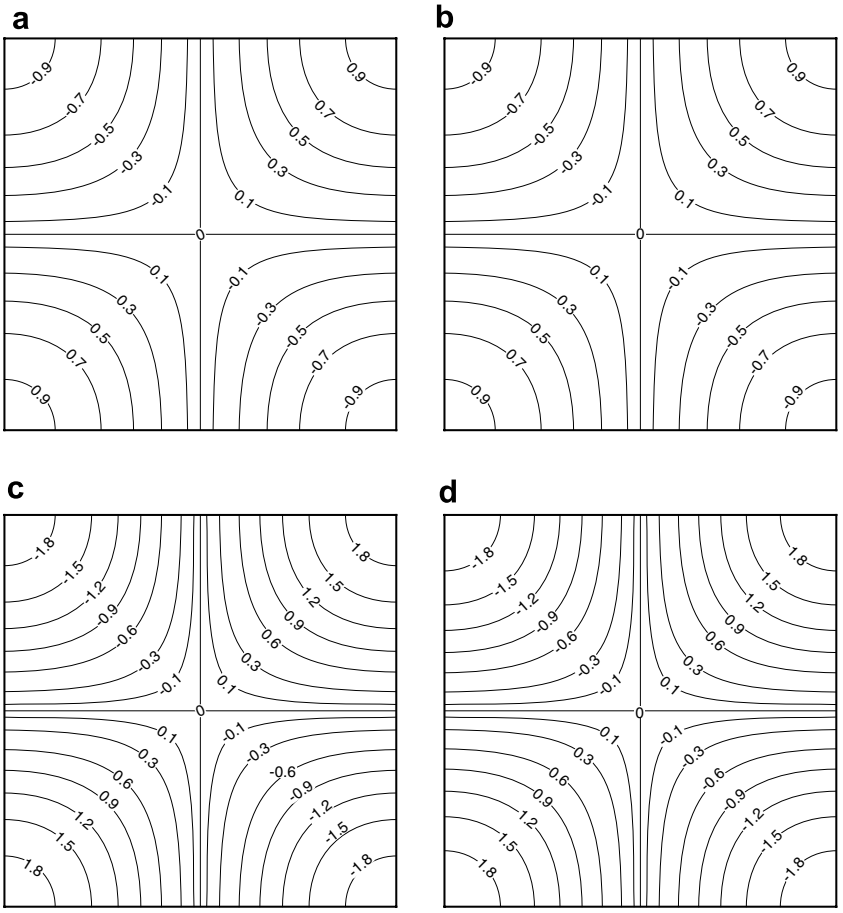

Fig. 3. For problem 1, at $t = 10$, $Re = 1000$, ($\Delta t = 0.01$, $\lambda = 0.5$), on grid size 81×81: streamlines (a) exact, (b) numerical, and vorticity contours (c) exact, (d) numerical.

4.2. Test case 2: The lid-driven square cavity problem

Next we consider the classical 2D lid-driven square cavity problem. This problem, over the years, has become the most frequently used benchmark problem for the assessment of numerical methods, particularly the steady-state solution of incompressible fluid flows governed by the N–S equations [4,5,7,13,19,20,24,25,37,43]. This problem is of great scientific interest because it displays almost all fluid mechanical phenomena [14,35,38] for incompressible viscous flows in the simplest of geometrical settings. The geometry and the boundary conditions have been shown in Fig. 4 where the top wall is moving and the remaining three walls are stationary. No-slip boundary conditions have been employed on all the four walls. The moving wall generates vorticity which diffuses inside the cavity and this diffusion is the driving mechanism of the flow. At high *Re*s, several secondary and tertiary vortices begin to appear, whose characteristics depend on the *Re*. Because of the presence of large gradients near the walls, we generate a centro-symmetric grid (see the physical plane in Fig. 5(a) and the corresponding uniform grid in the computational plane in 5(b)) with clustering near the walls using the stretching functions

$$x = \xi - \frac{\lambda}{2\pi}\sin(2\pi\xi), \tag{22}$$

$$y = \eta - \frac{\lambda}{2\pi}\sin(2\pi\eta), \tag{23}$$

where λ is the stretching parameter with $0 \leqslant \lambda < 1$, as defined in problem 1.

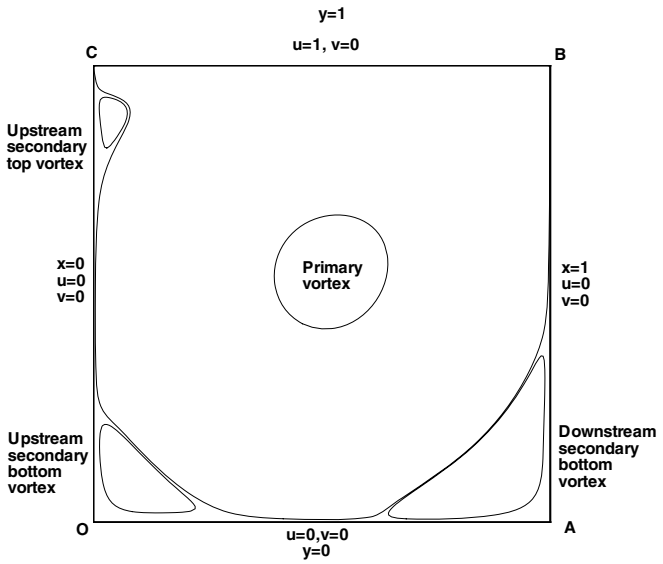

Fig. 4. The lid-driven cavity flow configuration with boundary conditions.

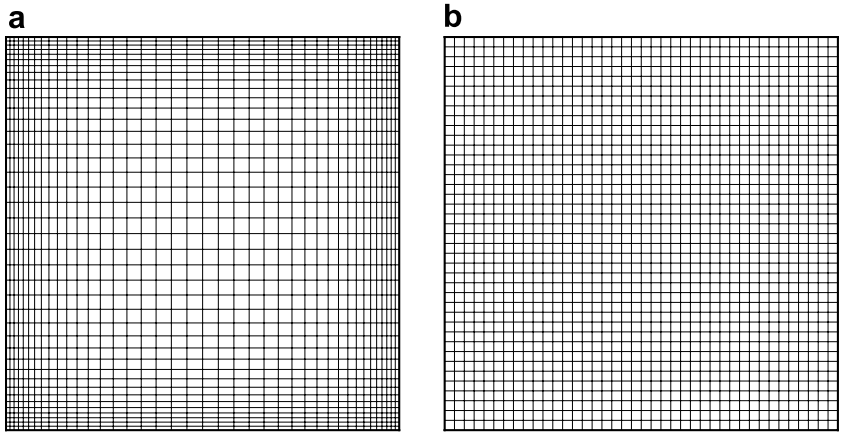

Fig. 5. The lid-driven square cavity flow problem, a typical 41×41 grid: (a) physical plane ($\lambda = 0.6$) and (b) computational plane.

4.2.1. Boundary conditions

Boundary conditions for velocity on the top wall is given by $u = 1$, $v = 0$. On all other walls of the cavity the velocities are zero ($u = v = 0$). In the ψ–ζ setting used here, streamfunction values on all the four walls are zero ($\psi = 0$).

Table 3
Lid-driven cavity flow problem: effect of the stretching parameter for $Re = 400$ on a 41×41 grid

λ	Present		Reference (Ghia et al.)	
	$\psi_{\min}$	$\zeta(0.5, 1)$	$\psi_{\min}$	$\zeta(0.5, 1)$
0.6	−0.112	−9.99162	−0.114	−10.0545
0.7	−0.111	−9.96032		
0.8	−0.110	−9.89285		
0.9	−0.108	−9.64820		

We now proceed to develop HOC wall boundary conditions for vorticity ζ in the following manner:

In the physical plane, the velocity on the left wall, where the index for x-direction is 0 and j is the y-direction index varying from 0 to $y_{\max}$, on using forward difference, we have

$$v_{0,j} = -\left.\frac{\partial\psi}{\partial x}\right|_{0,j} = -\delta_x^+\psi_{0,j} + \frac{\Delta x}{2}\left.\frac{\partial^2\psi}{\partial x^2}\right|_{0,j} + \frac{(\Delta x)^2}{6}\left.\frac{\partial^3\psi}{\partial x^3}\right|_{0,j} + \mathrm{O}((\Delta x)^3), \tag{24}$$

where Δx is the distance between the left wall and the first point closest to it in the physical plane. Using the fact that $\dfrac{\partial^2\psi}{\partial y^2} = 0$ on a vertical wall, from the Poisson Eq. (6), we have

$$\left.\frac{\partial^2\psi}{\partial x^2}\right|_{0,j} = -\zeta_{0,j}, \quad \left.\frac{\partial^3\psi}{\partial x^3}\right|_{0,j} = -\left.\frac{\partial\zeta}{\partial x}\right|_{0,j} = -\frac{1}{x_\xi}\delta_\xi^+\zeta_{0,j}. \tag{24a}$$

Table 4
Lid-driven cavity flow problem: grid independence study of the steady-state data at the center of the cavity

Re	Present					Reference			
	Grid	Velocity		ψ	ζ	Grid	Velocity		ζ
		u	v				u	v	
100	21	−0.20424	0.05489	−0.06468	−1.12383	129	−0.20581 [13]	0.05454 [13]	–
	31	−0.20690	0.05636	−0.06566	−1.15113	–	–	–	–
	41	−0.20785	0.05688	−0.06600	−1.16012	–	–	–	–
	61	−0.20851	0.05729	−0.06619	−1.16404	–	–	–	–
	81	−0.20882	0.05738	−0.06641	−1.17101	89	–	–	−1.17442 [31]
1000	41	−0.07180	0.02810	−0.10858	−2.01270	–	–	–	–
	61	−0.06469	0.02638	−0.11463	−2.05634	–	–	–	–
	81	−0.06304	0.02600	−0.11585	−2.06441	–	–	–	–
	101	−0.06253	0.02587	−0.11622	−2.06661	160	−0.06206 [5]	0.02578 [5]	−2.06722 [5]
	121	−0.06189	0.02582	−0.11587	−2.05344	–	–	–	–

Table 5
Steady-state primary vortex data for the lid-driven cavity flow for $100 \leqslant Re \leqslant 5000$

Re	Variables	Ghia et al. [13] (1982)	Kim and Moin [24] (1985)	Bruneau and Saad [7] (2005)	Present ($\lambda = 0.6$)
100	$\psi_{\min}$	−0.103	−0.103		−0.103
	$\zeta_{v,c}$	−3.166	−3.177	–	−3.1397
	x, y	(0.6172, 0.7344)	–	–	(0.6183, 0.7273)
	Grid	129×129	65×65	–	41×41
400	$\psi_{\min}$	−0.114	−0.112	–	−0.1135
	$\zeta_{v,c}$	−2.295	−2.260	–	−2.2920
	x, y	(0.5547, 0.6055)	–	–	(0.5532, 0.6055)
	Grid	257×257	65×65	–	61×61
1000	$\psi_{\min}$	−0.118	−0.116	−0.1189	−0.1183
	$\zeta_{v,c}$	−2.050	−2.026	−2.0674	−2.0659
	x, y	(0.5313, 0.5625)	–	(0.5313, 0.5654)	(0.5399, 0.5598)
	Grid	129×129	97×97	1024×1024	81×81
2000	$\psi_{\min}$	–	–	–	−0.1182
		–	–	–	(−0.120) [17]
	$\zeta_{v,c}$	–	–	–	−1.9453
	x, y	–	–	–	(0.5200, 0.5598)
	Grid	–	–	–	81×81
3200	$\psi_{\min}$	−0.120	−0.115	–	−0.1193
	$\zeta_{v,c}$	−1.989	−1.901	–	−1.9399
	x, y	(0.5165, 0.5469)	–	–	(0.5160, 0.5479)
	Grid	129×129	97×97	–	101×101
5000	$\psi_{\min}$	−0.119	−0.112	−0.1219	−0.1204
	$\zeta_{v,c}$	−1.860	−1.812	−1.9322	−1.9708
	x, y	(0.5117, 0.5352)		(0.5147, 0.5352)	(0.5133, 0.5399)
	Grid	257×257	97×97	1024×1024	121×121

Using the above results and $v_{0,j} = 0$ (as the vertical velocity on the left wall is zero) with $\Delta x = x_\xi \mathrm{d}\xi + x_\eta \mathrm{d}\eta = h x_\xi$ ($\because x_\eta = 0$, $\mathrm{d}\xi = h$ in the computational plane), (24) can be written in the computational plane as

Table 6
Steady-state secondary and tertiary vortex data for the lid-driven cavity flow for $100 \leqslant Re \leqslant 5000$

Vortex	Property	*Re*				
		100	400	1000	3200	5000
Secondary	$\psi_{\max}$	–	–	–	5.91e−4	1.27e−3
TL		–	–	–	(7.28e−4)	(1.46e−3)
	Location x, y	–	–	–	0.0491, 0.8988	0.0624, 0.9101
		–	–	–	(0.0547, 0.8984)	(0.0625, 0.9125)
	H_L	–	–	–	0.0838	0.1153
		–	–	–	(0.0859)	(0.1211)
	V_L	–	–	–	0.2054	0.2678
		–	–	–	(0.2057)	(0.2693)
BL	$\psi_{\max}$	2.06e−6	1.37e−5	2.12e−4	8.92e−4	1.23e−3
		(1.75e−6)	(1.42e−5)	(2.31e−4)	(9.78e−4)	(1.36e−3)
	Location x, y	0.0316, 0.0316	0.0528, 0.0439	0.0840, 0.0727	0.0794, 0.1175	0.0727, 0.1384
		(0.0313, 0.0391)	(0.0508, 0.0469)	(0.0859, 0.0781)	(0.0859, 0.1094)	(0.0703, 0.1367)
	H_L	0.0834	0.1301	0.2288	0.3002	0.3310
		(0.0781)	(0.1273)	(0.2188)	(0.2844)	(0.3184)
	V_L	0.0835	0.1093	0.1665	0.2462	0.2840
		(0.0781)	(0.1081)	(0.1680)	(0.2305)	(0.2643)
BR	$\psi_{\max}$	1.22e−5	6.35e−4	1.75e−3	2.85e−3	3.16e−3
				(1.73e−3)*		(3.07e−3)*
		(1.25e−5)	(6.42e−4)	(1.75e−3)	(3.14e−3)	(3.08e−3)
	Location x, y	0.9526, 0.0638	0.8908, 0.1233	0.8616, 0.1092	0.8247, 0.0863	0.8005, 0.0782
				(0.8643, 0.1123)*		(0.8057, 0.0732)*
		(0.9453, 0.0625)	(0.8906, 0.1250)	(0.8594, 0.1094)	(0.8125, 0.0859)	(0.8086, 0.0742)
	H_L	0.1334	0.2723	0.3191	0.3589	0.3816
		(0.1328)	(0.2617)	(0.3034)	(0.3406)	(0.3565)
	V_L	0.1612	0.3193	0.3685	0.4204	0.4457
		(0.1484)	(0.3203)	(0.3536)	(0.4102)	(0.4180)
Tertiary	$\psi_{\min}$	–	–		−5.87e−8	−2.16e−8
BL		–	–	–	(−6.33e−8)	(−7.08e−8)
	Location x, y	–	–	0.0059, 0.0060	0.0080, 0.0080	0.0060, 0.0080
		–	–	–	(0.0078, 0.0078)	(0.0117, 0.0078)
	H_L	–	–	0.0156	0.0168	0.0152
		–	–	–	(0.0254)	(0.0156)
	V_L	–	–	0.0175	0.0160	0.0165
		–	–	–	(0.0234)	(0.0163)
Tertiary	$\psi_{\min}$	−1.25e−9	−4.81e−8	−1.10e−7	−2.77e−7	−1.26e−6
BR		–	(−8.91e−8)	(−9.32e−8)	(−2.52e−7)	(−1.46e−6)
	Location x, y	0.9974,0.0057	0.9933, 0.0067	0.9933, 0.0067	0.9879, 0.0121	0.9795, 0.0170
			(0.9922, 0.0078)	(0.9922, 0.0078)	(0.9844, 0.0078)	(0.9805, 0.0195)
	H_L	0.0081	0.0152	0.0078	0.0240	0.0559
		–	(0.0156)	(0.0078)	(0.0254)	(0.0528)
	V_L	0.0075	0.0156	0.0087	0.0226	0.0448
		–	(0.0156)	(0.0078)	(0.0234)	(0.0417)
Grid Size (present)		41×41	61×61	61×61	101×101	121×121
Ghia et al.		(129×129)	(257×257)	(129×129)	(129×129)	(257×257)
*Bruneau and Saad	–	–	–	(1024×1024)	–	(1024×1024)

$$0 = -\frac{1}{x_\xi}\delta_\xi^+\psi_{0,j} - \frac{1}{2}hx_\xi\zeta_{0,j} - \frac{1}{6}h^2x_\xi\delta_\xi^+\zeta_{0,j} + \mathrm{O}(h^3). \tag{25}$$

Vorticity at the left wall ($\zeta_{0,j}$) can be easily obtained from Eq. (25). The vorticity at the other boundaries can be approximated in a similar way.

We now present the transient and the time-marching steady-state solutions produced by the proposed scheme for this problem in Tables 3–7 and Figs. 6–14. Table 3 shows the effect of the stretching parameter λ where it is seen that with increasing λ, the minimum streamfunction value and the vorticity at the mid-point of the moving wall deviate from the benchmark results of reference [13]. This is due to the fact that severe clustering at the walls takes away some significant points from the interior and high-gradient vorticity regions are not necessarily aligned to the walls [13]. Therefore, for most of the computations for this problem, we have used $\lambda = 0.6$. Fig. 6 shows the good effects of clustering: Fig. 6(a) and (b) respectively show computed steady-

Table 7
Convergence data and relaxation parameter for the lid-driven square cavity problem on a 61×61 grid in a PC with Pentium 4 processor and 512 MB RAM

Re	CPU (s)	Relaxation parameter (inner (ζ), inner (ψ))
100	116.585 (64.926)	(0.725, 0.9)
400	261.197 (126.972)	(0.425, 0.625)
1000	782.034 (372.254)	(0.5,0.6)

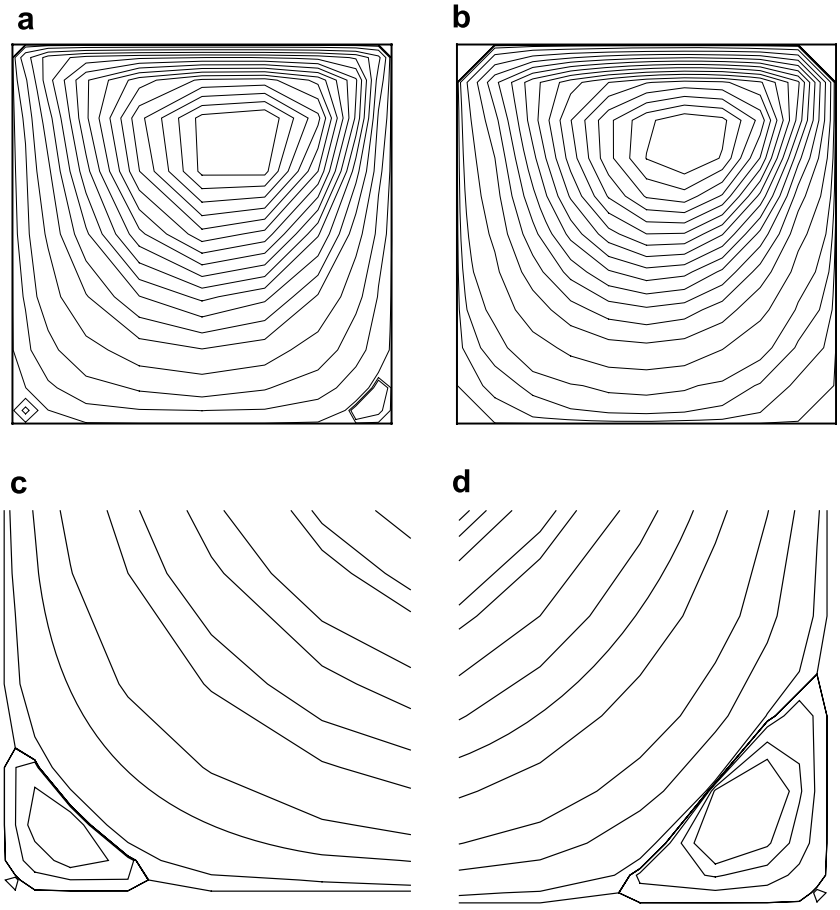

Fig. 6. The lid-driven square cavity flow problem, $Re = 100$: streamlines computed on a 11×11 grid with (a) the present scheme ($\lambda = 0.7$), (b) Ref. [40]; appearance of tertiary vortex on a 21×21 grid ($\lambda = 0.95$): (c) bottom left and (d) bottom right.

state streamlines for $Re = 100$ on clustered non-uniform ($\lambda = 0.7$) and a uniform 11×11 grid. It is clear that without clustering the vicinity of the walls, a uniform grid cannot produce the secondary corner vortices at the bottom. Likewise Fig. 6(c) and (d) show the bottom left and bottom right corners of the cavity, where a grid as coarse as 21×21 was able to resolve even the tertiary vortices for this Reynolds number.

In Fig. 7, we present comparisons of the horizontal velocities on the vertical centerline and the vertical velocities on the horizontal centerline of the square cavity for Reynolds numbers ranging from 100 to 5000 and compare our data with those of Ghia et al. [13]. While the data for [13] was obtained using 129×129 and 257×257 grids, our data is obtained using a 21×21 grid ($Re = 100$), a 41×41 grid ($Re = 400$), a 81×81 grid ($Re = 1000$), 101×101 grid ($Re = 3200$) and a 121×121 grid ($Re = 5000$). In each case, our velocity profiles exhibit a perfect match with Ghia's results.

In Fig. 8, we compare our data of the horizontal vorticities along the vertical centerline and the vertical vorticities along the horizontal centerline of the square cavity on a grid 61×61 for Reynolds number 1000 with those of [7] on a grid 1024×1024. Bruneau and Saad have used 1024×1024 grid for $Re = 1000$, whereas same results are reproduced by the proposed scheme on a grid as coarse as 61×61. The close agreement revealed between these two results indicates that the present scheme is much more superior than some recent schemes [22,26,28].

In Fig. 9, we exhibit the well known streamlines for $100 \leqslant Re \leqslant 5000$ while Fig. 10 contains the corresponding vorticity contours. All of these graphs exhibit the typical separations and secondary vortices at the bottom corners of the cavity as well as at the top left of the square cavity.

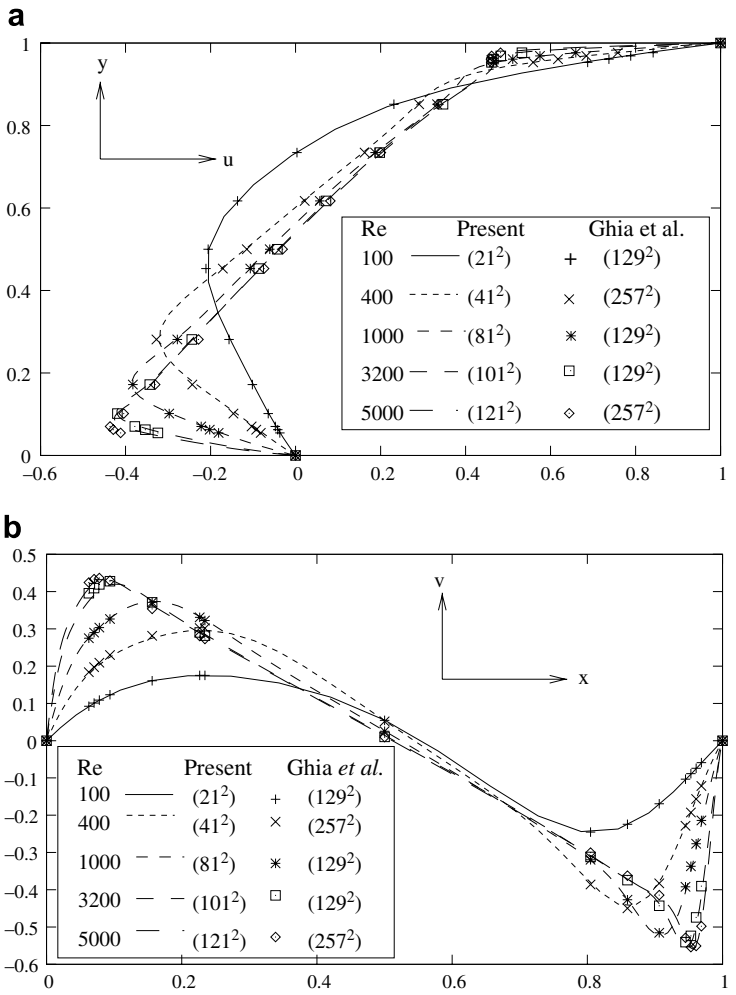

Fig. 7. The lid-driven square cavity flow problem: comparison of steady-state (a) horizontal velocity along the vertical centerline and (b) vertical velocity along the horizontal centerline from $Re = 100$ to $Re = 5000$.

In Table 4, we present our grid independence data for u, v, ψ and ζ for $Re = 100$ and 1000, and compare them with those of Refs. [5,13,31]. Table 5 compares our primary vortex data for $100 \leqslant Re \leqslant 5000$ with the benchmark results of [13] as well as other published results [7,17,24]. In Table 6, we provide the secondary and tertiary vortex data for the same range of Reynolds numbers and compare them with those of [7,13] (values given within parentheses). In all cases our results exhibit an excellent match with all the references cited above.

In Figs. 11 and 12, we show the time-wise evolution of the streamlines for $Re = 1000$ and 3200 till the steady-state is reached (on a 81×81 and 101×101 grid respectively). These figures show that our scheme excellently captures the formation of the secondary and tertiary vortices as time progresses. In a similar note, the adjacent tables show the time evolution of the ψ–ζ data at different time stations for $Re = 1000$ and 3200 respectively on a 81×81 and 101×101 grid. We have compared the transient data presented in Fig. 11 with the same given in [11].

Figs. 13 and 14 respectively show the horizontal velocity along the vertical centerline and vertical velocity along the horizontal centerline at instant $t = 20.0$ captured with three different time steps $\Delta t = 0.05$, 0.01 and 0.001 for $Re = 5000$. These profiles captured on a grid of size 121×121 clearly exemplifies the good effects of the implicitness of our scheme which allows time step as coarse as $\Delta t = 0.05$ to achieve time-grid-independence (hence time-accuracy).

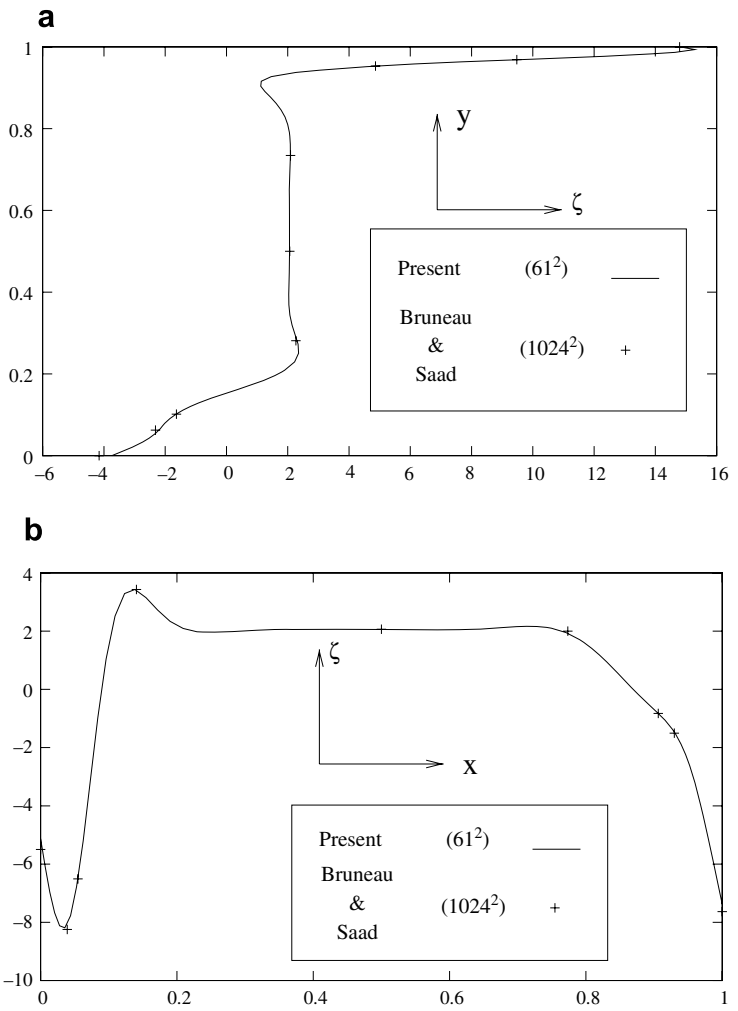

Fig. 8. The lid-driven square cavity flow problem: comparison of steady-state (a) horizontal vorticity along the vertical centerline and (b) vertical vorticity along the horizontal centerline for $Re = 1000$.

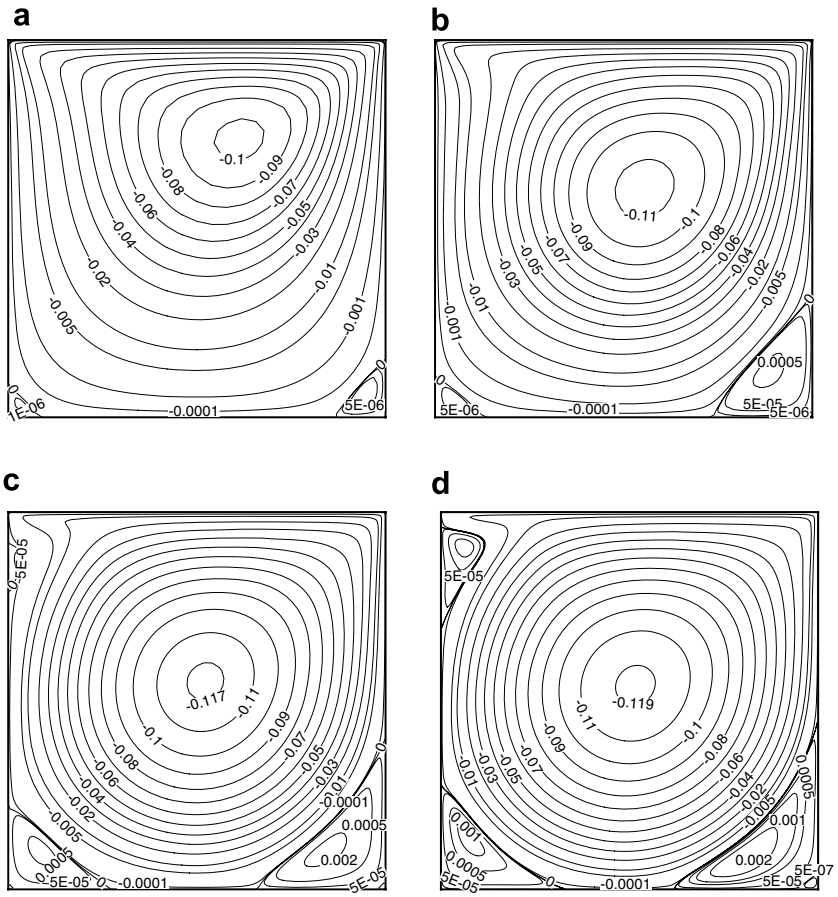

Fig. 9. The lid-driven square cavity flow problem: comparison of steady-state stream-function contours for different *Re*s with $\lambda = 0.6$: (a) $Re = 100$ on (41×41), (b) $Re = 400$ on (61×61), (c) $Re = 2000$ on (81×81) and (d) $Re = 5000$ on (121×121).

In Table 7, we present the convergence data (and CPU time) on a 61×61 grid till steady-state where steady-state was assumed to reach when

$$\max |\zeta^{(n+1)} - \zeta^{(n)}| < 5 \times 10^{-6}.$$

Here, $\zeta^{(n+1)}$ and $\zeta^{(n)}$ stand for solutions at $(n+1)$th and nth time steps respectively and we have used the computed solution for a lower *Re* as the initial guess for a higher *Re*. We also compare our CPU times with that for the scheme presented in [19], which used direct discretization on a uniform Cartesian grid. Although the CPU time taken by our scheme is more than the CPU time taken for direct discretization on a uniform Cartesian grid (presented here within parentheses), our scheme has the advantage of working equally well in domains beyond rectangular whereas the scheme in [19] is limited to rectangular domain only. It is worthwhile mentioning that coarser uniform grid used in [19] could not capture the flow patterns for higher *Re*s accurately.

4.3. Test case 3: Constricted channel

A classic problem for studying the flow past a re-entrant corner is the flow in a non-uniform channel containing a step-down constriction [6,33,34] (see Fig. 15) in which the shape of the channel boundary can vary from a smooth constriction (Fig. 16(a)) to one with a very sharp but smooth corner (Fig. 16(b)). At such a corner the flow becomes singular and in particular, vorticity becomes infinite [33]. For accurate resolution of the flow at this location, the downstream requires more grid refinement compared to the upstream. We construct such a grid using the conformal mapping [33,34]:

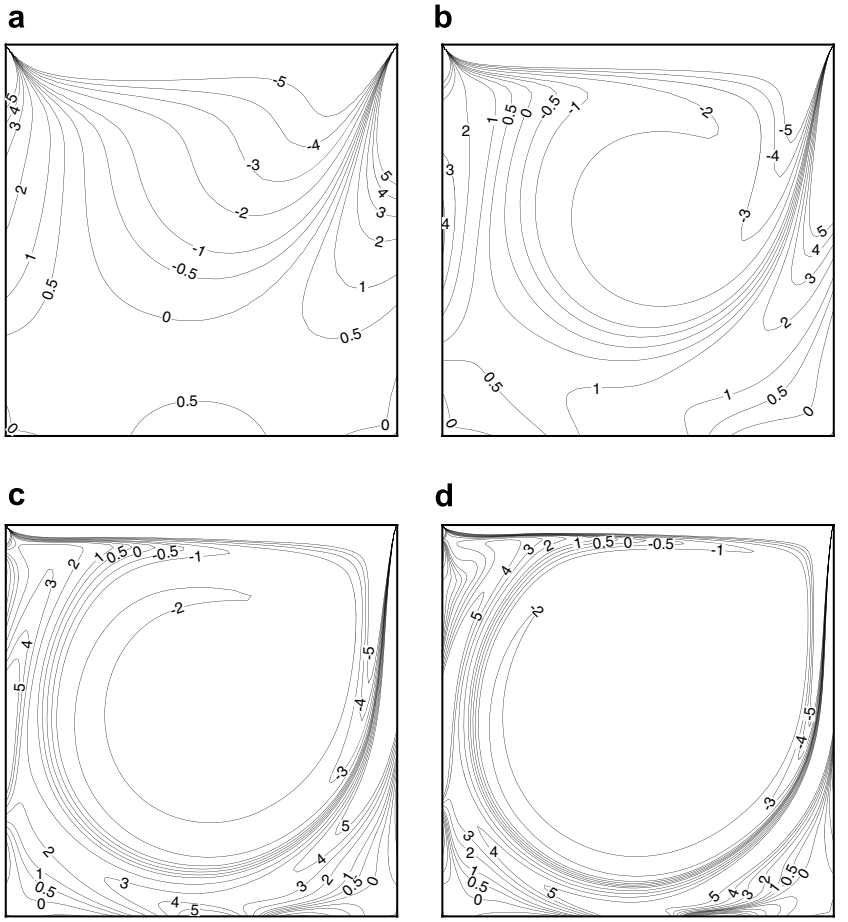

Fig. 10. The lid-driven square cavity flow problem: comparison of steady-state vorticity contours for different *Re*s with $\lambda = 0.6$: (a) $Re = 100$ on (41×41), (b) $Re = 400$ on (61×61), (c) $Re = 2000$ on (81×81) and (d) $Re = 5000$ on (121×121).

$$z = w(A + B\tanh(w)), \tag{26}$$

where $z = x + \mathrm{i}y$ and $w = \xi + \mathrm{i}\eta$ $(\mathrm{i} = \sqrt{-1})$ with

$$x = A\xi + \frac{B}{H}[\xi\sinh(2\xi) - \eta\sin(2\eta)], \tag{27}$$

$$y = A\eta + \frac{B}{H}[\eta\sinh(2\xi) + \xi\sin(2\eta)]. \tag{28}$$

Here, $H = \cosh(2\xi) + \cos(2\eta)$; A and B are constants defined by $A = \dfrac{l_\mathrm{i} + l_\mathrm{o}}{2\tau}$, $B = \dfrac{l_\mathrm{o} - l_\mathrm{i}}{2\tau}$ where $2l_\mathrm{i}$, $2l_\mathrm{o}$ respectively are the inlet and outlet heights of the constricted channel and τ is a parameter controlling smoothness as well as sharpness of the constriction: an increasing value of τ indicating a more sharp corner. In the present computation, we have taken $l_\mathrm{i} = 1$ and $l_\mathrm{o} = 0.5$.

The flow here is axisymmetric and the governing equations are as given in (6) and (7). It is well known that the choice of the inlet and outlet boundary locations affects the behaviour of flow. We made a few test runs to determine the optimal inlet (and outlet) distance from the throat such that the throat effect becomes negligible at the inlet (and outlet). Eventually, we have fixed the distance of the inlet boundary at $x = -15$ and the outlet boundary at $x = 25$.

We introduce a Poiseuille profile at the inlet and fully developed flow conditions at the outlet. We also use no-slip conditions at the upper wall which translate to $\psi_\eta = 0$ and $\psi =$ constant (which is taken as 1 here) in the computational plane; at the central line $\psi = 0$, $\zeta = 0$.

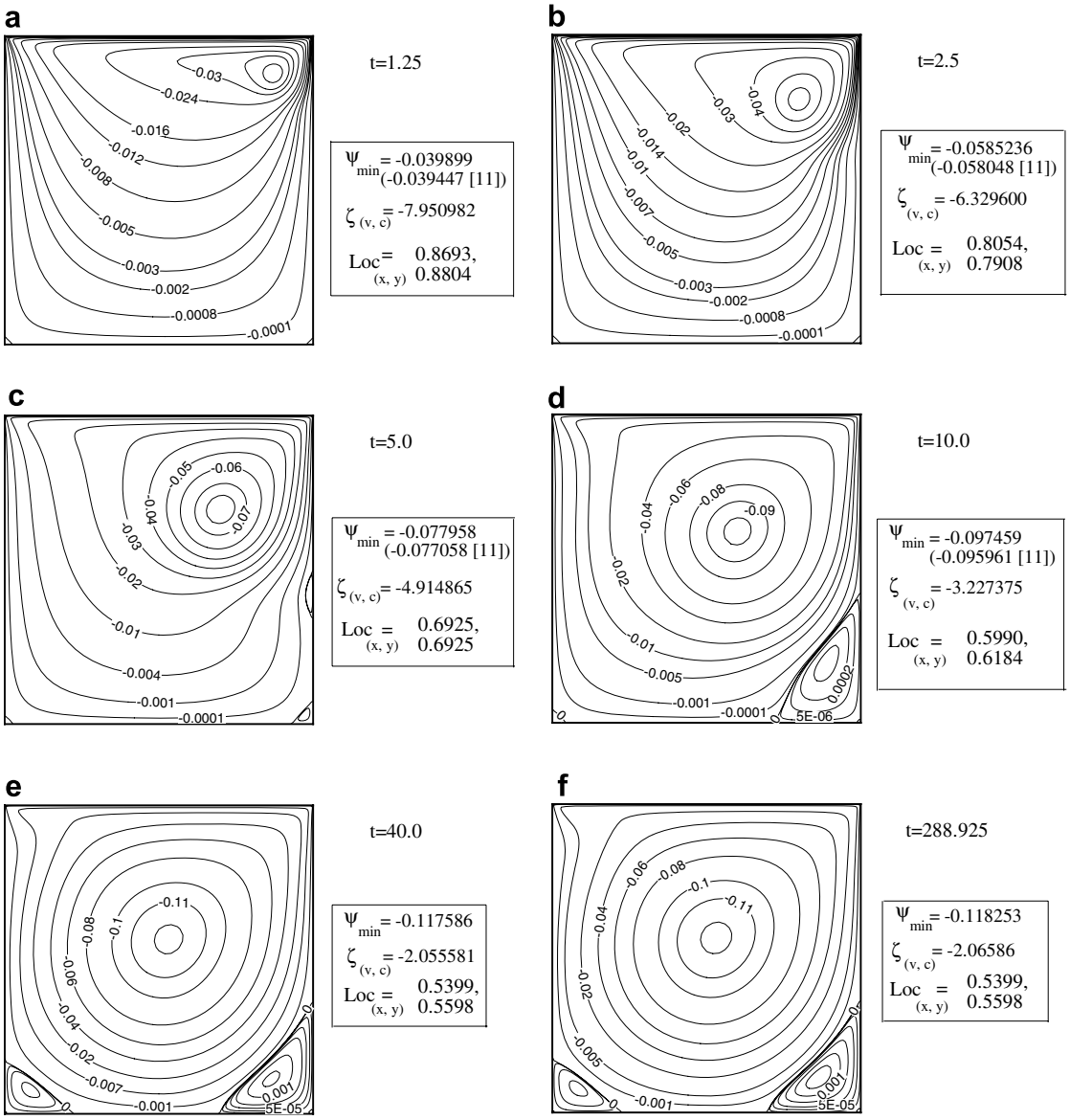

Fig. 11. Evolution of streamlines at different time stations for the lid-driven cavity flow for $Re = 1000$ on a grid 81×81 ($\lambda = 0.6$): (a) $t = 1.25$, (b) $t = 2.5$, (c) $t = 5.0$, (d) $t = 10.0$, (e) $t = 40.0$ and (f) $t = 288.925$ (steady-state).

As no analytical solution exists for the problem, in order to estimate the grid convergence rate for this problem, we compute the steady-state solution on three different grid sizes 161×16, 321×31 and 641×61 (denoted by C, M and F respectively). Then the formula for grid convergence rate of a variable ϕ (which represents u, v, ψ or ζ here) is

$$\alpha_R = \frac{\ln((\|\phi^M - \phi^C\|_\infty)/(\|\phi^F - \phi^M\|_\infty))}{\ln 2}, \tag{29}$$

where

$$\|\phi^F - \phi^M\|_\infty = \max_{i,j} |\phi^F_{i,j} - \phi^M_{i,j}|. \tag{30}$$

We present these results in Table 8 for three Reynolds numbers, namely, 1, 10, 100. All the flow variables show approximately a fourth order grid convergence as expected. We have compared our computed grid convergence rate based on maximum error with those in [34] (presented here within parentheses).

For this problem, there is no quantitative results available in the existing literature. Therefore we compare our qualitative results, namely the streamfunction contours with those obtained by Mancera. Our streamline patterns are very similar to those in [33,34]. In Fig. 16(a) and (b), we show the grids used for $\tau = 0.6$ and 1.0 respectively. Fig. 17(a) and (b) respectively show the streamlines for Reynolds numbers 500 and 750 in the channel with $\tau = 0.6$ whereas Fig. 17(c) and (d) show the same for Reynolds numbers 250 and 500 with $\tau = 1.0$. One can see from the last two figures that even for lower Reynolds

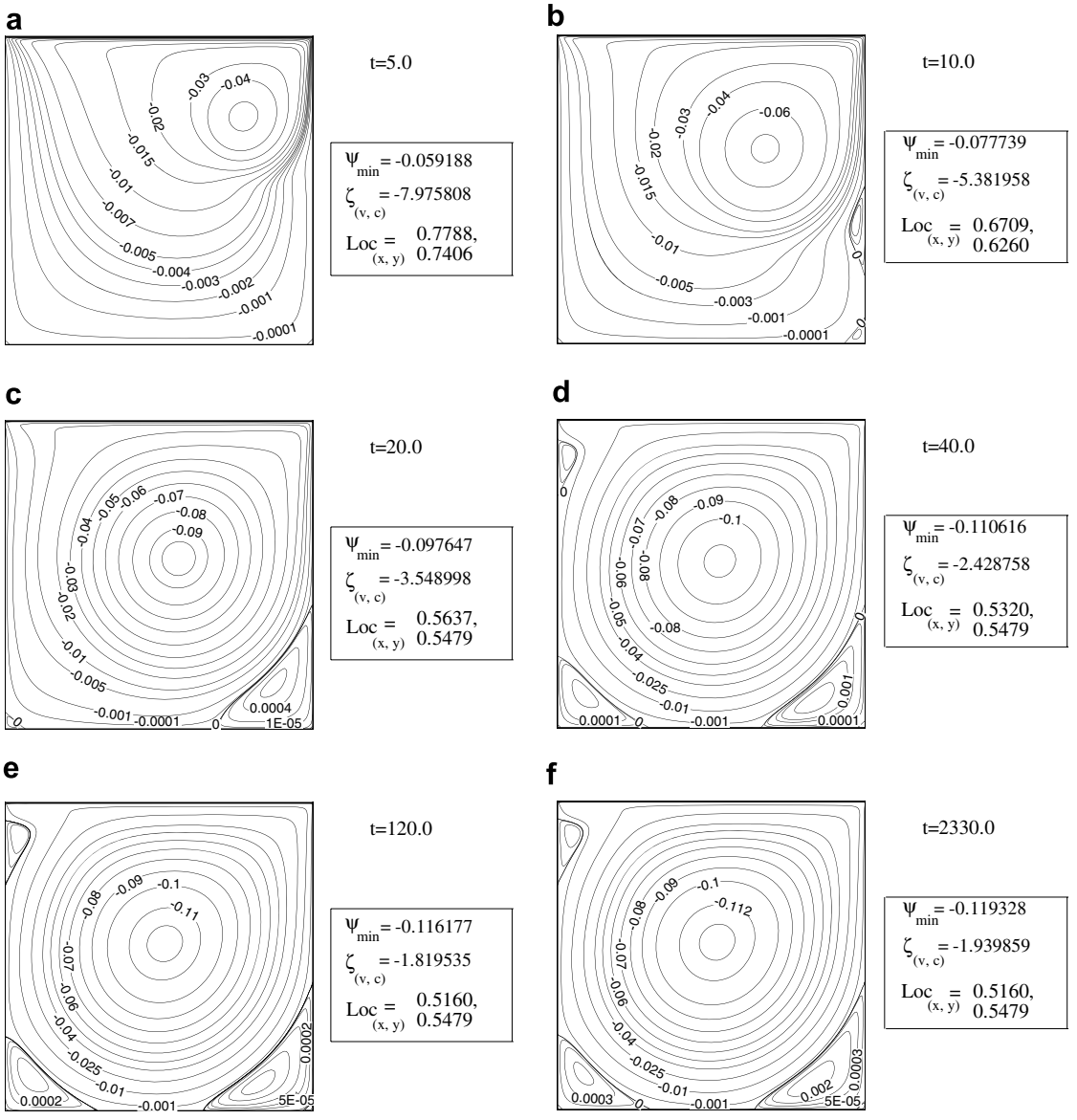

Fig. 12. Evolution of streamlines at different time stations for the lid-driven cavity flow for $Re = 3200$ on a grid 101×101 ($\lambda = 0.6$): (a) $t = 5.0$, (b) $t = 10.0$, (c) $t = 20.0$, (d) $t = 40.0$, (e) $t = 120.0$ and (f) $t = 2330.0$ (steady-state).

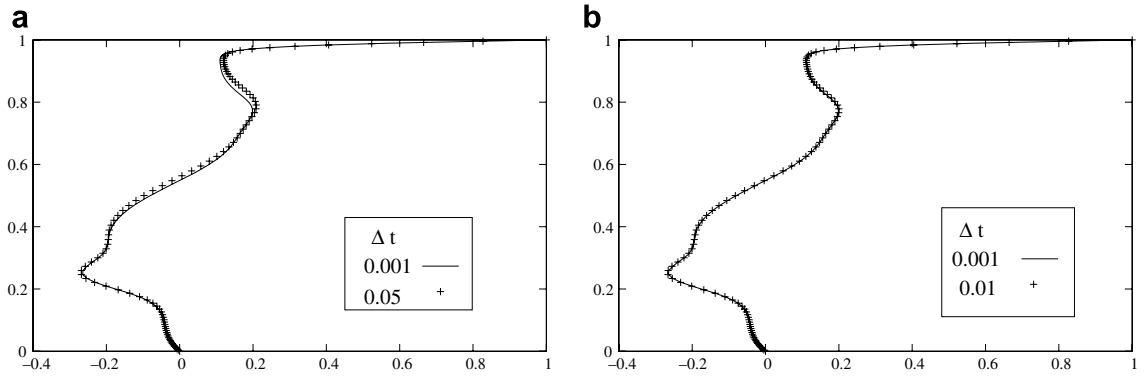

Fig. 13. Temporal grid independence study, horizontal velocity along the vertical centerline for $Re = 5000$ at time station $t = 20$ (λ=0.6) for lid-driven cavity flow: (a) $\Delta t = 0.001$, 0.05 and (b) $\Delta t = 0.001$, 0.01.

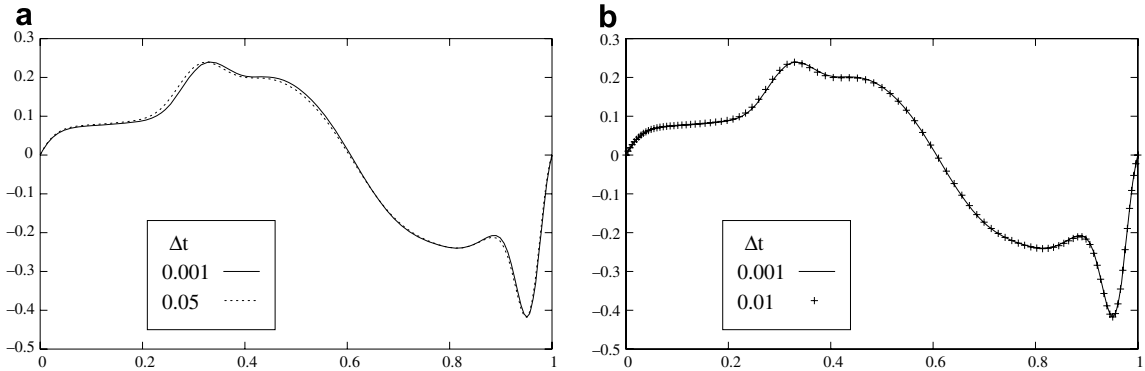

Fig. 14. Temporal grid independence study, vertical velocity along the horizontal centerline for $Re = 5000$ at time station $t = 20$ ($\lambda = 0.6$) for lid-driven cavity flow: (a) $\Delta t = 0.001$, 0.05 and (b) $\Delta t = 0.001$, 0.01.

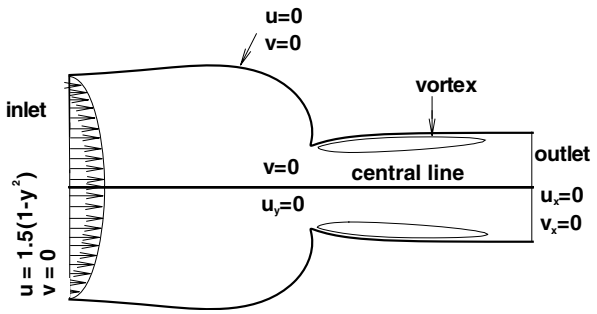

Fig. 15. Constricted channel flow configuration with boundary conditions.

numbers typical flow separation occurs for higher values of τ. These figures also show that the size and strength of the vortex in the region just after the corner increase with increasing *Re*s. It is heartening to note that the scheme in [34] could not achieve a converged solution for $Re = 500$, and $\tau = 1.0$ whereas our computation produces a well converged solution for the same *Re*.

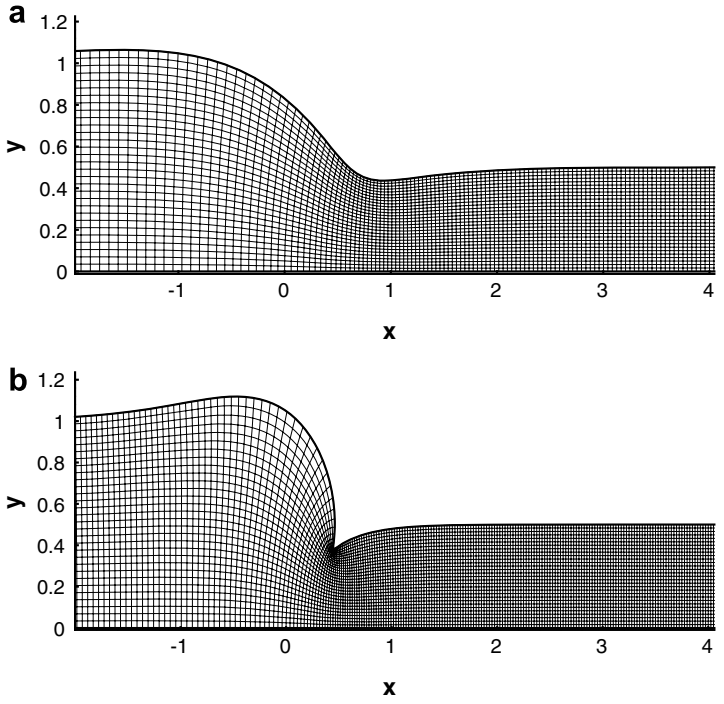

Fig. 16. Close-up view of grid used for the constricted channel flow: (a) 301×16 ($\tau = 0.6$) and (b) 601×31 ($\tau = 1.0$).

Table 8
Error analysis of the constricted channel flow problem for different *Re*s ($\tau = 0.6$)

Re		Errors		Rate
		$\|\phi^M - \phi^C\|_\infty$	$\|\phi^F - \phi^M\|_\infty$	
1.0	ψ	1.705187e−03	1.111000e−04	3.94
	ζ	1.124975e−02	7.101000e−04	3.43
	u	2.822500e−03	7.080000e−04	3.99
	v	3.531502e−03	2.238000e−04	3.98
10.0	ψ	3.060635e−03	2.008000e−04	3.93 (3.60 [34])
	ζ	2.208857e−02	1.371000e−03	4.01 (3.75 [34])
	u	1.892129e−02	1.232800e−03	3.94
	v	1.216307e−02	7.870000e−04	3.95
100.0	ψ	8.086469e−03	6.353000e−04	3.67 (1.48 [34])
	ζ	4.897917e−02	2.998200e−03	4.03 (3.69 [34])
	u	8.545852e−02	7.047700e−03	3.60
	v	5.004434e−02	4.070300e−03	3.62

5. Conclusions

In this paper, we introduce a new HOC formulation for solving unsteady incompressible viscous flow problems in 2D governed by the N–S equations on non-rectangular physical domains on orthogonal grids. Our scheme is implicit, second order accurate in time and fourth order accurate in space. Both Dirichlet and Neumann boundary conditions can be easily incorporated into the scheme. The use of BiCGStab algorithm for solving the algebraic systems arising at every time level, makes the implicit procedure computationally

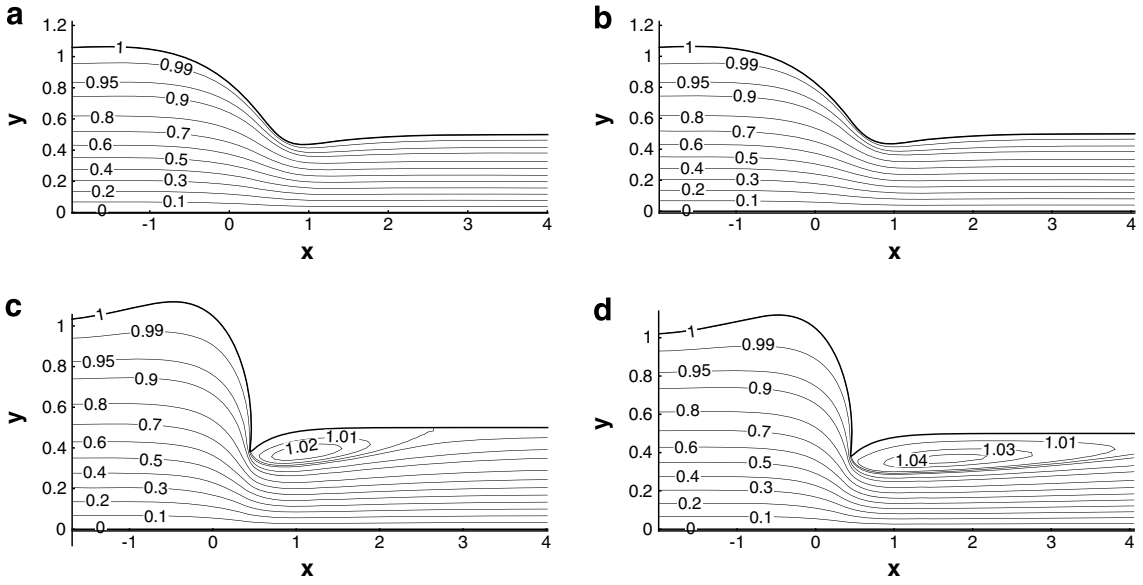

Fig. 17. For the constricted channel flow problem: close-up view of streamlines for $\tau = 0.6$, (a) $Re = 500$, (b) $Re = 750$, and for $\tau = 1.0$, (c) $Re = 250$, (d) $Re = 500$.

efficient even in capturing transient solutions. Since the proposed scheme is higher order accurate, it demands lesser number of grid points than other popular schemes to reach the desired accuracy. To bring out different aspects of the scheme, we employed it to compute the transient solutions of the flow decayed by viscosity, the time-marching steady-state solution of the 2D lid-driven cavity flow and more importantly, to the constricted channel flow problem. We have addressed several issues relating to the use of HOC schemes on stretched, rectangular and curvilinear meshes. Our scheme can be used for curvilinear coordinates also. The robustness of the scheme is illustrated by its applicability to problems of varying physical complexities, represented among others, by Reynolds numbers ranging from 100 to 5000 in the cavity problem and 1 to 750 in the channel problem. The results obtained in all the test cases on relatively coarser grids are in excellent agreement with the analytical as well as the established numerical results, underlining the high accuracy of the scheme. The implicit nature of the scheme is fully exploited in arriving at the steady-state results for the lid-driven cavity and the constricted channel problem, where time-steps as high as 0.1 have been employed for some of the computations. The strength of the scheme can be easily realized from the fact that on non-uniform 11×11 grids the secondary and on 21×21 grids the tertiary vortices can be clearly visualized even for $Re = 100$. As our scheme has the added advantage of being applicable to non-rectangular physical domains, it has very good potential for efficient computation of incompressible viscous flows on complex geometries.

References

[1] J.H. Ferziger, M. Peric, Computational Methods for Fluid Dynamics, Springer, 2002.
[2] M.R. Visbal, D.V. Gaitonde, D.P. Rizzetta, High-order schemes for DNS/LES and CAA on curvilinear dynamic meshes, in: DNS/LES Progress and Challenges, Greyden Press, 2001, ISBN 1-57074-488-2. August.
[3] F. Auteri, L. Quartapelle, L. Vigevano, Accurate ψ–ζ spectral solution of the singular driven cavity problem, J. Comput. Phys. 180 (2002) 597–615.
[4] E. Barragy, G.F. Carey, Stream function–vorticity driven cavity solution using p finite elements, Comput. Fluids 26 (5) (1997) 453–468.
[5] O. Botella, R. Peyret, Benchmark spectral results on the lid-driven cavity flow, Comput. Fluids 27 (1998) 421–433.
[6] A. Brüger, B. Gustafsson, P. Lötstedt, J. Nilsson, High order accurate solution of the incompressible Navier Stokes equations, J. Comput. Phys. 203 (2005) 49–51.
[7] C.H. Bruneau, M. Saad, The 2D lid-driven cavity problem revisited, Comput. Fluids 35 (2005) 326–348.

[8] J.E. Castillo, S. Steinberg, The sensitivity and accuracy of fourth order finite-difference schemes on nonuniform grids in one dimension, DE-AC04-76DP00789, 1995.
[9] Y.N. Chen, S.C. Yang, J.Y. Yang, Implicit weighted essentially non-oscillatory schemes for the incompressible Navier–Stokes equations, Int. J. Numer. Methods Fluids 31 (1999) 747–765.
[10] A.J. Chorin, Numerical solution of the Navier–Stokes equation, Math. Comput. 22 (1968) 747–762.
[11] V.V. Chudanov, A.G. Popkov, A.G. Churbanov, P.N. Vabishchevich, M.M. Makarov, Operator-splitting schemes for the streamfunction–vorticity formulation, Comput. Fluids 24 (7) (1995) 771–786.
[12] L. Ge, J. Zhang, Accuracy iterative solution of convection diffusion equation with boundary layers on nonuniform grids, Technical Report, University of Kentucky, Lexington, KY, No. 288-99, 1999.
[13] U. Ghia, K.N. Ghia, C.T. Shin, High-*Re* solutions for incompressible Navier–Stokes equation and a multigrid method, J. Comput. Phys. 48 (1982) 387–411.
[14] J.W. Goodrich, K. Gustafson, K. Halasi, Hopf bifurcation in the driven cavity, J. Comput. Phys. 90 (1990) 219–261.
[15] M.M. Gupta, R.M. Manohar, J.H. Stephenson, A single cell high order scheme for the convection–diffusion equation with variable coefficients, Int. J. Numer. Methods Fluids 4 (1984) 641–651.
[16] M.M. Gupta, High accuracy solutions of incompressible Navier–Stokes equations, J. Comput. Phys. 93 (1991) 343–357.
[17] S. Hou, Q. Zou, S. Chen, G. Doolen, A. Cogley, Simulation of cavity flows by the lattice Boltzmann method, J. Comput. Phys. 118 (1995) 329–347.
[18] J.D. Hoffman, Relationship between the truncation errors of centered finite-difference approximations on uniform and nonuniform meshes, J. Comput. Phys. 46 (1982) 469–474.
[19] J.C. Kalita, D.C. Dalal, A.K. Dass, A class of higher order compact schemes for the unsteady two-dimensional convection–diffusion equation with variable convection coefficients, Int. J. Numer. Methods Fluids 38 (2002) 1111–1131.
[20] J.C. Kalita, A.K. Dass, D.C. Dalal, A transformation-free HOC for steady convection–diffusion on nonuniform grids, Int. J. Numer. Methods Fluids 44 (2004) 33–53.
[21] J.C. Kalita, D.C. Dalal, A.K. Dass, Fully compact higher order computation of steady-state natural convection in a square cavity, Phys. Rev. E 64 (6) (2001) 066703 (1–13).
[22] T. Kawamura, H. Takami, K. Kuwahara, A new high order upwind scheme for incompressible Navier–Stokes equations, Lect Notes Phys. 218 (1985).
[23] C.A. Kennedy, M.H. Carpenter, Several new numerical methods for compressible shear-layer simulations, Appl. Numer. Math. 14 (2) (1994) 397–433.
[24] J. Kim, P. Moin, Application of fractional step method to incompressible Navier–Stokes equation, J. Comput. Phys. 59 (1985) 308–323.
[25] J.R. Koseff, R.L. Street, The lid-driven cavity flow: A synthesis of qualitative and quantitative observations, ASME J. Fluids Eng. 106 (1984) 390–398.
[26] R.A. Kupferman, A central-difference scheme for a pure stream function formulation of incompressible viscous flows, SIAM J. Sci. Comput. 23 (1) (2001) 1–18.
[27] S.K. Lele, Compact finite difference schemes with spectral like resolution, J. Comput. Phys. 103 (1992) 16–42.
[28] B.P. Leonard, The ULTIMATE conservative difference scheme applied to unsteady one-dimensional advection, Comput. Methods Appl. Mech. Eng. 88 (1) (1991) 17–74.
[29] M. Li, T. Tang, B. Fornberg, A compact fourth order finite difference scheme for the steady incompressible Navier–Stokes equations, Int. J. Numer. Methods Fluids 20 (1995) 1137–1151.
[30] M. Li, T. Tang, A compact fourth order finite difference scheme for unsteady viscous incompressible flows, SIAM J. Sci. Comput. 16 (1) (2001) 29–45.
[31] P. Luchini, Higher-order difference approximations of the Navier–Stokes equations, Int. J. Numer. Methods Fluids 12 (1991) 491–506.
[32] R.J. Mackinnon, R.W. Johnson, Differential equation based representation of truncation errors for accurate numerical solution, Int. J. Numer. Methods Fluids 13 (1991) 739–757.
[33] P.F.A. Mancera, R. Hunt, Fourth order method for solving the Navier Stokes equations in a constricted channel, Int. J. Numer. Methods Fluids 25 (1997) 1119–1135.
[34] P.F.A. Mancera, A study of numerical solution of the steady two dimensional Navier–Stokes equations in a constricted channel problem by a compact fourth order method, Appl. Math. Comput. 146 (2003) 771–790.
[35] M.K. Moffat, Viscous and resistive eddies near a sharp corner, J. Fluid Mech. 18 (1964) 1–18.
[36] Y.V.S.S. Sanyasiraju, V. Manjula, Higher order semi compact scheme to solve transient incompressible Navier–Stokes equations, Comput. Mech. 35 (2005) 441–448.
[37] R. Schreiber, H.B. Keller, Driven cavity flows by efficient numerical techniques, J. Comput. Phys. 49 (1983) 310–333.
[38] P.N. Shankar, M.D. Deshpande, Fluid mechanics in the driven cavity, Annu. Rev. Fluid Mech. 32 (2000) 93–136.
[39] W.F. Spotz, G.F. Carey, Formulation and experiments with high-order compact schemes for nonuniform grids, Int. J. Numer. Methods Heat Fluid Flow 8 (3) (1998) 288–303.
[40] W.F. Spotz, G.F. Carey, High-order compact scheme for the steady stream-function vorticity equations, Int. J. Numer. Methods Eng. 38 (1995) 3497–3512.
[41] J.C. Strikwerda, High-order accurate schemes for incompressible viscous flow, Int. J. Numer. Methods Fluids 24 (1997) 715–734.
[42] H. Van Der Vorst, BiCGSTAB : a fast and smoothly converging variant of BiCG for the solution of nonsymmetric linear systems, SIAM J. Sci. Comput. 13 (1992) 631–644.

[43] S.P. Vanka, Block-implicit multigrid solution of Navier–Stokes equations in primitive variables, J. Comput. Phys. 65 (1986) 138–158.
[44] M. Yanwen, F. Dexun, T. Kobayashi, N. Taniguchi, Numerical solution of the incompressible Navier–Stokes equations with an upwind compact difference scheme, Int. J. Numer. Methods Fluids 30 (1999) 509–521.